ACS Sustainable Chemistry & Engineering

pubs.acs.org/journal/ascecg

Research Article

Investigation into the Reaction Pathways and Catalyst Deactivation for Polyethylene Hydrogenolysis over Silica-Supported Cobalt Catalysts

Siddhesh S Borkar,‡ Ryan Helmer,‡ Suraj Panicker, and Manish Shetty*

Cite This: *ACS Sustainable Chem. Eng.* 2023, 11, 10142−10157

Read Online

ACCESS | Metrics & More | Article Recommendations | Supporting Information

ABSTRACT: Chemical repurposing has emerged as a promising route to valorize "end-of-use" plastic waste and mitigate its release to the environment. In this work, we applied silica-supported cobalt (5 wt % Co/SiO_2) catalysts to produce liquid-range hydrocarbons (C_5−C_{30}) in the batch phase at 200−300 °C, 20−40 bar H_2, and 2−36 h with high selectivity and investigated the reaction pathways, the influence of catalyst phase on the product yields and selectivity, and the catalyst deactivation mechanisms. Reaction conditions were optimized for improving liquid product yields at 275 °C, 30 bar H_2, and 8 h reaction time, giving a 55% liquid product yield (C-mole basis), comprising 75% of nonsolid products, with gas yields limited to ~19%. By tracking product evolution over time and with varying cobalt surface density, we propose a multipathway mechanism, including a dominant, nonterminal C−C cleavage route on the polymer chain over the catalyst, which drives the high liquid product selectivity. The catalyst also showed recyclability over four reactions with reduced activity and a shift in yield toward liquid products after the first reaction. It was effectively regenerated by calcination under air at 450 °C. We combined the reactivity data with powder X-ray diffraction (PXRD), thermogravimetric analysis coupled with mass spectrometry (TGA-MS), and catalyst surface areas via N_2 physisorption of various fresh, spent, recycled, and regenerated catalysts to attribute the reduced activity and selectivity shift mainly to the presence of a recalcitrant polymer species embedded on the catalyst, comprising 10.5−18.5 wt % of the spent catalyst, which obstructs access to active sites and increases liquid selectivity and overshadows the influence of carbonaceous coke or catalyst phase reduction to Co. Moreover, we successfully applied the catalyst to various postconsumer polyethylene (HDPE and LDPE) samples. These results move the field toward more sustainable and economically viable catalysts for the chemical upcycling of waste plastics.

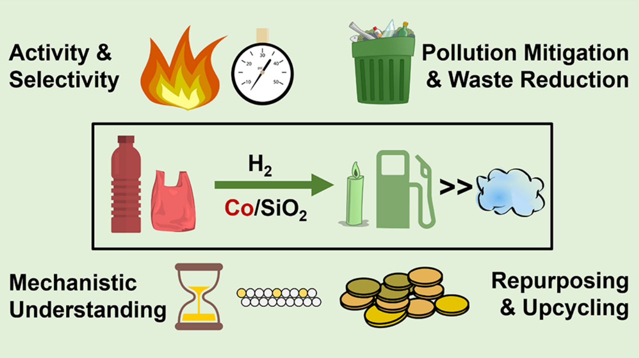

KEYWORDS: *Plastics upcycling, polyolefins, polyethylene, cobalt oxide, base metals, circular economy*

■ INTRODUCTION

Plastic production has grown exponentially over the past few decades, reaching ~400 MMt in 2017, and it is estimated to triple by 2050.[1,2] The enormous amount of plastics produced and circulated around the world in various forms has created a vast carbon footprint, and their improper disposal has led to growing environmental concerns. Over their lifecycle, plastics generated ~1.8 billion tons of CO_2 equivalents of greenhouse gases (GHGs) in 2019, which accounted for 3.4% of global emissions.[3−5] Crucially, at "end-of-use", plastics are typically sent to landfills or incinerated. A significant fraction invariantly leaks into the environment, disrupting various ecosystems primarily due to their long biodegradation times.[4,6−9] As such, moving away from the current linear life of plastics, which transmits fossil-based monomers to ultimate disposal into the environment, toward a circular plastic economy has become crucial.[3]

Currently, less than 9% of the disposed of plastics are recycled.[1] Mechanical recycling is the contemporary method of recycling plastics, but this avenue often leads to the degradation of the polymers' properties, resulting in a cyclic loss of value and eventual disposal by landfilling or incineration.[10] Chemical repurposing poses an alternative recycling pathway. We have previously reviewed the recent progress made along these routes in repurposing plastic waste.[11]

Received: April 18, 2023
Revised: June 9, 2023
Published: June 27, 2023

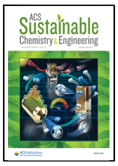

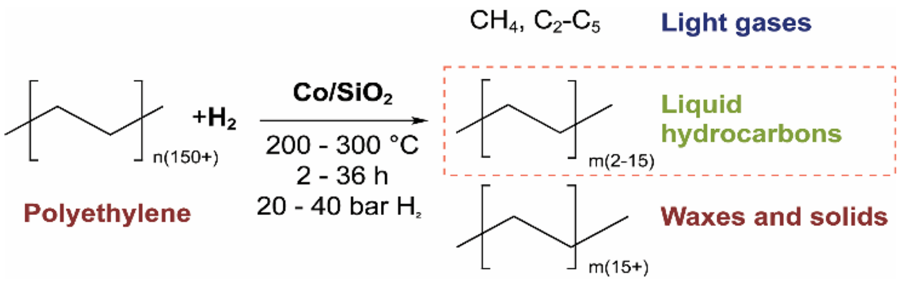

Figure 1. Hydrogenolysis of polyethylene over Co/SiO_2 at mild conditions.

Polyolefins (POs) are the most abundantly produced family of plastics, accounting for more than one-half of the global plastic production in 2020.[12] Therefore, within chemical repurposing, chemical transformations to efficiently depolymerize the most commonly produced polyolefins are desired, including low-density polyethylene (LDPE), high-density polyethylene (HDPE), and polypropylene (PP). The chemical inertness of the C(sp^3)−C(sp^3) bonds in the backbone of POs makes them especially challenging.[13] Hydrogenolysis has emerged as a promising technique to convert POs into a range of liquid and gas products that can be used as fuels, lubricants, and waxes.[3,5,14−16] While zirconium (Zr)-based materials were the first reported hydrogenolysis catalysts, ruthenium (Ru) and platinum (Pt) have emerged as two of the most active noble metals for depolymerizing POs, including recent work in quantitatively comparing the liquid selectivity of Ru on various supports.[17,18,16,19−25,3,7,26−33] While these Ru- and Pt-based catalysts have shown significant promise in producing drop-in replacements for fuels and lubricants, thereby reducing our dependence on virgin fossil sources, the scarcity and subsequent cost of such constrained resources, in turn, foment environmental challenges, societal struggles, and questions of long-term sustainability.[34,35] Alternate base-metal-based catalysts are needed to effectively exploit hydrogenolysis toward catalytic depolymerization of POs. Among the base metals, Ni supported on silica (Ni/SiO_2) has recently been studied by Vlachos and co-workers in deconstructing LDPE substrates to *n*-alkanes.[36] Co/ZSM-5 catalyst was reported by Román-Leshkov and co-workers to produce propane selectively compared to other supported Co catalysts.[37] Co supported on silica−alumina (SiO_2−Al_2O_3), SiO_2, CeO_2, ZrO_2, and TiO_2 showed little activity with predominantly solid products, while bulk Co_3O_4 produced mainly methane (CH_4). More recently, mesoporous SiO_2-supported ZrO_2 nanoparticles were shown to yield up to 86% liquid-range hydrocarbons from the hydrogenolysis of polyethylene (M_w = 90 000 g/mol).[38] While these studies have recognized the promise of earth-abundant metals as alternatives to the noble-metal catalysts, achieving a high selectivity of lucrative products, especially liquid-phase products over gaseous CH_4, with such catalysts remains an important challenge to address for achieving practical feasibility. Indeed, even while these base-metal materials like Co are encumbered with their supply chain challenges and resource constraints, scientific investigations on their catalytic capacities, such as those mentioned above and that presented here, will aid in moving the chemical industry away from the social, political, and environmental hurdles associated with precious metals like Pt toward more sustainable methods overall. Furthermore, detailed investigations exploring the hydrogenolysis reaction pathways and mechanisms, the role of active sites, catalyst phases, and support, and the mechanisms of deactivation remain elusive and are crucial for the effective utilization of the hydrogenolysis pathway for chemically repurposing plastics.

In this work, we have studied silica-supported base-metal cobalt (Co/SiO_2) catalysts for selectively converting PE substrates into a wide range of liquid and gas hydrocarbons under relatively mild conditions of 200−300 °C, 20−40 bar H_2 pressure, and 2−36 h reaction time, investigated the reaction pathways for PE hydrogenolysis, and identified the deactivation mechanisms. Figure 1 shows a schematic overview of the hydrogenolysis reaction of polyethylene. We probed the gas and liquid products and found individual hydrocarbon yields at varying reaction times to elucidate the terminal and nonterminal nature of the C−C bond cleavage. We also explored the effectiveness of the catalyst for various postconsumer polyolefin samples, including LDPE bottles and bags, an HDPE can, and a PP cup. We investigated the catalyst's reusability and regenerability at 300 °C, 30 bar H_2 pressure, and 4 h reaction time and interrogated the catalyst's active phase during the reaction via *postreaction* powder X-ray diffraction (PXRD). Finally, we probed the reasons for the change in catalyst activity when reused by surface area measurements using N_2 adsorption−desorption isotherms and thermogravimetric analysis coupled with mass spectrometry (TGA-MS) on spent catalyst samples.

■ RESULTS AND DISCUSSION

We tested an initial series of redox-inert silica (SiO_2)-supported transition-metal catalysts (Co, Fe, Pd, Pt, and Ru; these catalysts are herein referred to as Co/SiO_2, Fe/SiO_2, Pd/SiO_2. Pt/SiO_2, and Ru/SiO_2) for the hydrogenolysis of *n*-octadecane (*n*-C_{18}), a model linear alkane, at 200 °C, 30 bar H_2, 2 h, and a catalyst-to-substrate ratio of 1:20 (2.0 g of *n*-C_{18}, 0.1 g of catalyst). PXRD patterns of the catalyst prereaction showed that the phases of the metals were Co_3O_4, Fe_2O_3, PdO, Pt, and RuO_2 at room temperature postcalcination. The target catalyst loading on SiO_2 was 5 wt % of the phase at room temperature (metal or metal−oxide basis). The synthesized catalysts had surface areas of 320 (Co/SiO_2), 382 (Fe/SiO_2), 334 (Pd/SiO_2), 341 (Pt/SiO_2), and 340 m^2/g (Ru/SiO_2). The PXRD patterns, the N_2 physisorption isotherms, and the textural properties of the catalysts are given in the Supporting Information (Figures S1 and S2 and Table S1). In line with previous reports by Vlachos and co-workers, Román-Leshkov and co-workers, and Szanyi and co-workers highlighting the hydrogenolysis activity of Ru,[16,20,39] Ru/SiO_2 completely converted *n*-C_{18} into CH_4 in ∼97% yield on a C-mol basis. At the same time, Pd/SiO_2 and Fe/SiO_2 showed negligible hydrogenolysis reactivity, i.e., C_1−C_{17} yields of <1 C-mol%. Pt/SiO_2 showed only ∼3% yields toward hydrogenolysis products from *n*-C_{18}. Notably, Pt is a widely used catalyst for

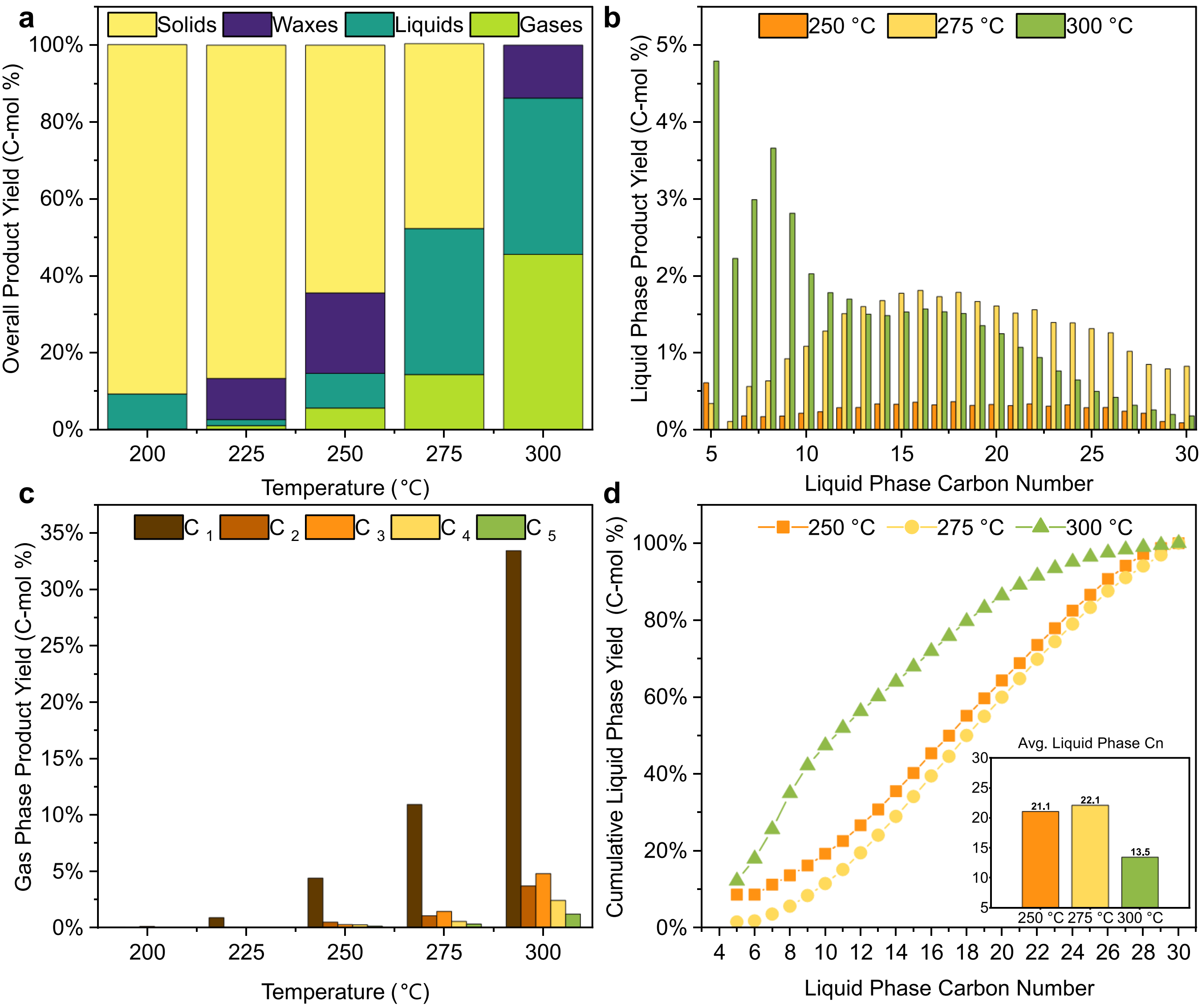

Figure 2. Effect of temperature on PE hydrogenolysis over Co/SiO_2. (a) Overall product yield (C-mol %), (b) liquid-phase product yield (C-mol %), (c) gas-phase product yield (C-mol %), and (d) cumulative liquid-phase product yield (C-mol %) and average liquid-phase carbon number (inset). Reaction conditions: 200−300 °C, 30 bar initial H_2, 4 h, 200 rpm, 1.0 g of PE, and 0.1 g of Co/SiO_2.

the hydrocracking of polyolefins on an acidic support.[3,7,26−28,30−32] Our data shows the lower propensity of Pt for hydrogenolysis on a redox-inert SiO_2 support. Interestingly, the base-metal Co/SiO_2 yielded ∼32% C_1−C_{17} alkanes from *n*-C_{18} (∼25% C_5−C_{17} liquid products and 7% C_1−C_5 gas products). The detailed product yields are given in Figure S3 and Table S2. Considering the potential of replacing noble-metal Ru catalysts with more base-metal Co catalysts, we selected Co/SiO_2 for further evaluation.

Thereafter, we investigated the effect of temperature on the hydrogenolysis of a model PE powder (M_w = 4000 g/mol, Sigma-Aldrich) on Co/SiO_2 between 200 and 300 °C to identify suitable reaction conditions for the hydrogenolysis of PE at ∼30 bar H_2 initial pressure for 4 h (Figure 2). At all temperatures, the products consisted of C_1−C_5 light alkanes (denoted as gases), C_5−C_{30+} alkanes (denoted as liquids and captured by gas chromatography, vide infra), solid residues (denoted as solids), and C_{30+} hydrocarbons (denoted as waxes). The waxes were ascribed to C_{30+} oligomers extracted from the solids in the postreaction workup but not detected in the gas chromatography (GC) results. As the products of interest were primarily in the gas and liquid phases and the solid residue could theoretically be further converted in a subsequent reaction, the solid residue was considered an indication of substrate conversion. In addition, the liquid product selectivity, among all products excluding solid residue, is used to indicate preference toward the desired liquid products. We note that the inherent subtleties in the melt−solid−gas nature of the reaction system result in catalyst contact and mass transfer challenges. As such, the discussion of the data here builds on the overarching trends elucidated from a holistic perspective of the results.

As shown in Figure 2a, the catalyst showed low conversion at 200 and 225 °C, as seen from the solid yield being greater than ∼87% at both temperatures. As the temperature was raised, the conversion of PE increased, as solid yields decreased from ∼87% at 225 °C to 0% at 300 °C. Importantly, the liquid product selectivity increased from 12% at 225 °C to a maximum of 72% at 275 °C and decreased to 41% at 300 °C (Table S5).

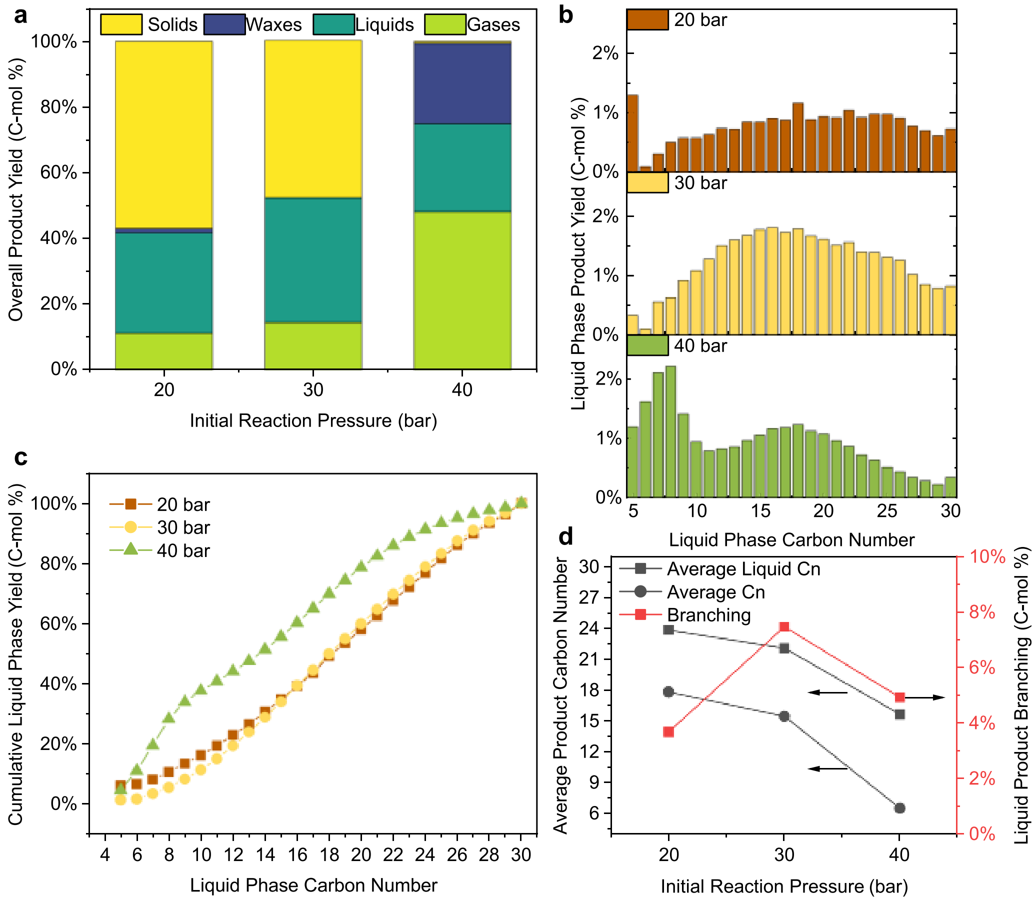

Figure 3. Effect of H_2 pressure on PE hydrogenolysis over Co/SiO_2. (a) Overall product yield (C-mol %), (b) liquid-phase product yield (C-mol %), (c) cumulative liquid-phase yield (C-mol %), and (d) branching and average product carbon numbers. Reaction conditions: 275 °C, 20−40 bar initial H_2, 4 h, 200 rpm, 1.0 g of PE, and 0.1 g of Co/SiO_2.

At all temperatures greater than 225 °C, CH_4 was the dominant gaseous product (Figure 2c) while the liquid-phase products were distributed across the entire range from C_5−C_{30}. Figure 2b shows the liquid-phase product distribution at 250, 275, and 300 °C. The product distributions at 250 and 275 °C were similar, with the latter temperature yielding ∼4 times more liquids (∼9% and ∼38% liquid yields, respectively). At 300 °C, along with complete conversion of the PE, a ∼41% yield to liquids and ∼46% yield to gases was observed (Figure 2a). Figure 2d presents the cumulative product yields in the liquid phase, with a given cumulative yield representing the aggregate yield of all products of lesser or equal carbon number, highlighting the total fraction of liquid products present in different carbon number ranges. This emphasizes the uniform product carbon distribution at 250 and 275 °C compared to the liquid phase at 300 °C concentrated at lower carbon numbers (Figure 2b). Specifically, ∼90% of the liquids at 300 °C were in the gasoline and diesel (C_5−C_{21}) range (Figure 2d) as compared to ∼60−70% at 250 and 275 °C. This was further reflected in the average liquid-phase carbon numbers of 21.1, 22.1, and 13.5 at 250, 275, and 300 °C, respectively (Figure 2d).

To evaluate the contributions of the SiO_2 support toward reactivity, we contacted PE with SiO_2 at 275 °C and compared its activity for PE hydrogenolysis with no catalyst (i.e., against a thermal PE hydrogenolysis) at the same temperature (Table S4). SiO_2 showed similar activity compared to no catalyst, albeit with greater liquid yields (16% vs 6%), suggesting a higher degree of PE conversion due to either the enhanced surface area (398 m^2/gm) and mild adsorption provided by the SiO_2 as compared to the reactor, or the mild catalytic activity of SiO_2 which may be attributed to its surface acidity- (supported by the prevalence of a significant fraction of branched liquid hydrocarbons as seen in Table S4).[40] In comparison, Co/SiO_2 enhanced PE conversion and the formation of liquid alkanes and suppressed product branching, demonstrating the efficacy of the supported catalyst toward PE hydrogenolysis (Figure S4).

Next, we investigated the PE hydrogenolysis reactivity of Co/SiO_2 at 275 °C between 20 and 40 bar initial H_2 pressure (at room temperature). A temperature of 275 °C was selected to compare the effect of H_2 pressure based on optimized liquid yields observed at 275 °C (Figure 2). As shown in Figure 3, the overall product yields marginally improved from 20 to 30 bar H_2. Specifically, gas yields increased from 11% to 14% and liquid yields increased from 31% to 38% as the H_2 pressure increased from 20 to 30 bar. The average total and liquid carbon numbers were between ∼16 and 18 and ∼22 and 24, respectively (Figure 3d) at 20−30 bar H_2. The liquid-phase product distribution was similar (Figure 3b). As the H_2 pressure was further increased to 40 bar, PE showed a much higher conversion (∼1% solid yield), and the gas-phase and liquid-phase yields were ∼48% and ∼27%, respectively. Notably, the liquid-phase distribution showed a higher yield of lower carbon numbers and a bimodal distribution (Figure 3b). The branched product fraction among the liquids was

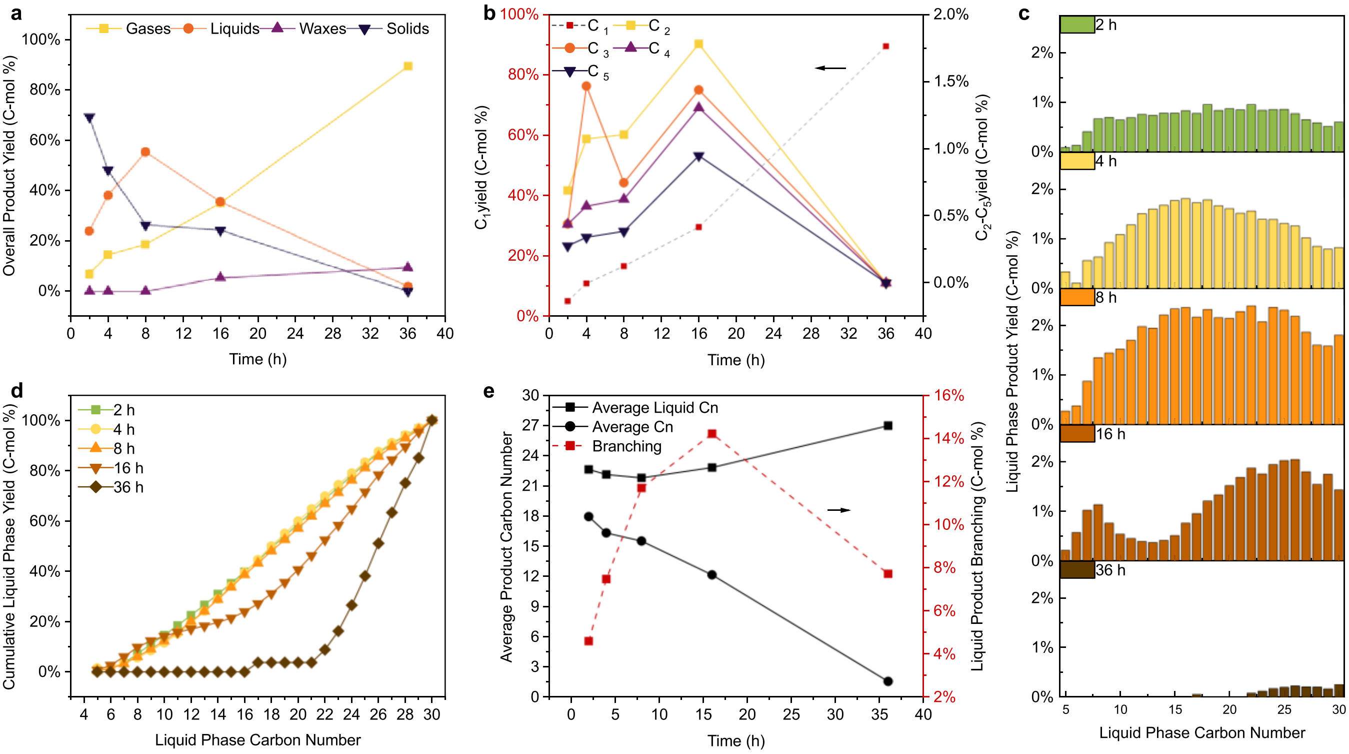

Figure 4. Effect of reaction time on PE hydrogenolysis over Co/SiO$_2$. (a) Overall product yield (C-mol %), (b) gas-phase product yields (C-mol %), (c) liquid-phase product yield (C-mol %), (d) cumulative liquid-phase yield (C-mol %), and (e) average product carbon numbers and liquid-phase product branching (C-mol %). Reaction conditions: 275 °C, 30 bar initial H$_2$, 2−36 h, 200 rpm, 1.0 g of PE, and 0.1 g of Co/SiO$_2$.

~4−7% at all H$_2$ pressures (Figure 3d). Interestingly, ~80% of total liquid carbons at 40 bar H$_2$ pressure were in the jet fuel and diesel range (C$_5$−C$_{21}$),[41] which was reflected in the lower average liquid-phase carbon number of ~16 as compared to an average liquid carbon number of ~22−24 at 20 and 30 bar H$_2$ pressures (Figure 3d).

The product distributions were tracked with varying reaction times to investigate the PE hydrogenolysis reaction pathway from 2 to 36 h at 275 °C and 30 bar initial H$_2$ pressure (Figure 4). Figure 4a shows that increasing the reaction time from 2 to 36 h increased the PE conversion, as solid yields fell from ~69% at 2 h to 0% at 36 h. The liquid yield increased from ~24% to ~55% as the time increased from 2 to 8 h and then decreased to ~35% and ~2% after 16 and 36 h, respectively. It is important to note that the liquid product selectivity remained similar at 78% at 2 h, 72% at 4 h, and 75% at 8 h, dropped to 47% at 16 h, and then decreased to 2% at 36 h as the products were ultimately converted to CH$_4$.

The liquid products showed a broad carbon number distribution from 2 to 8 h (Figure 4c). At 16 h, the liquid product distribution was bimodal with peaks in the gasoline (C$_5$−C$_{12}$) and motor-oil (C$_{22}$−C$_{30}$) ranges.[41] As shown in Figure 4d, between 2 and 16 h, 40−50% of liquid products were in the gasoline and diesel-fuel range with the rest in the motor-oil (C$_{22}$−C$_{30}$) range. This was also reflected in the average liquid-phase carbon number, which was consistently between ~22 and 24 (Figure 4e). The percentage of branched hydrocarbons in the liquid phase increased monotonically from ~4% to ~15% from 2 to 16 h.

In contrast to the liquids, the gas yield steadily increased with the reaction time, from 7% at 2 h to ~89% at 36 h (Figure 4a). Concomitantly, the average carbon number of the product dropped from an initial value of ~18 at 2 h to ~1.5 at 36 h. Intriguingly, in the gas phase, the yield of C$_2$−C$_5$ peaked at 16 h and then dropped to 0% at 36 h while the CH$_4$ yield increased continually (Figure 4b). Interestingly, the propane (C$_3$) yield at 4 h was higher than the corresponding ethane (C$_2$) yield, in line with a previous report highlighting the selective production of C$_3$ over a Co/ZSM-5 catalyst,[37] further indicating nonterminal C−C cleavage at intermediate conversion.

Based on the C−C bond cleavage location along the PE backbone, we hypothesize that the hydrogenolysis reaction can take several possible parallel routes (Figure 5). First, in the *terminal* C−C cleavage route, the terminal C−C bond at the ends of the polyolefin chains can undergo dehydrogenative adsorption on the metal site followed by C−C cleavage, which forms CH$_4$ and the polyolefin with one less carbon atom, which all then desorb from the surface. The polymer chain end can then progressively be cleaved with successive events, steadily increasing the CH$_4$ yield. Furthermore, this route alone would produce only CH$_4$ and solids at low reaction times, with liquid products only appearing late when the polyolefins have been repeatedly trimmed to the oligomer range.

On the other hand, the *sequential nonterminal* cleavage route (Figure 5) involves dehydrogenative adsorption of random, internal C−C bonds away from the chain ends, forming fragmented polyolefin chains as the primary products, which then desorb. After that, successive events independently can occur on the daughter polyolefin chains, forming a variety of hydrocarbons, which eventually form CH$_4$ as the products are cleaved further. Assuming statistical randomness of the C−C bond adsorption, various products can be formed, initially dominated by shortened, solid-phase polymer chains and some gas- and liquid-range hydrocarbons. Liquid phase oligomers

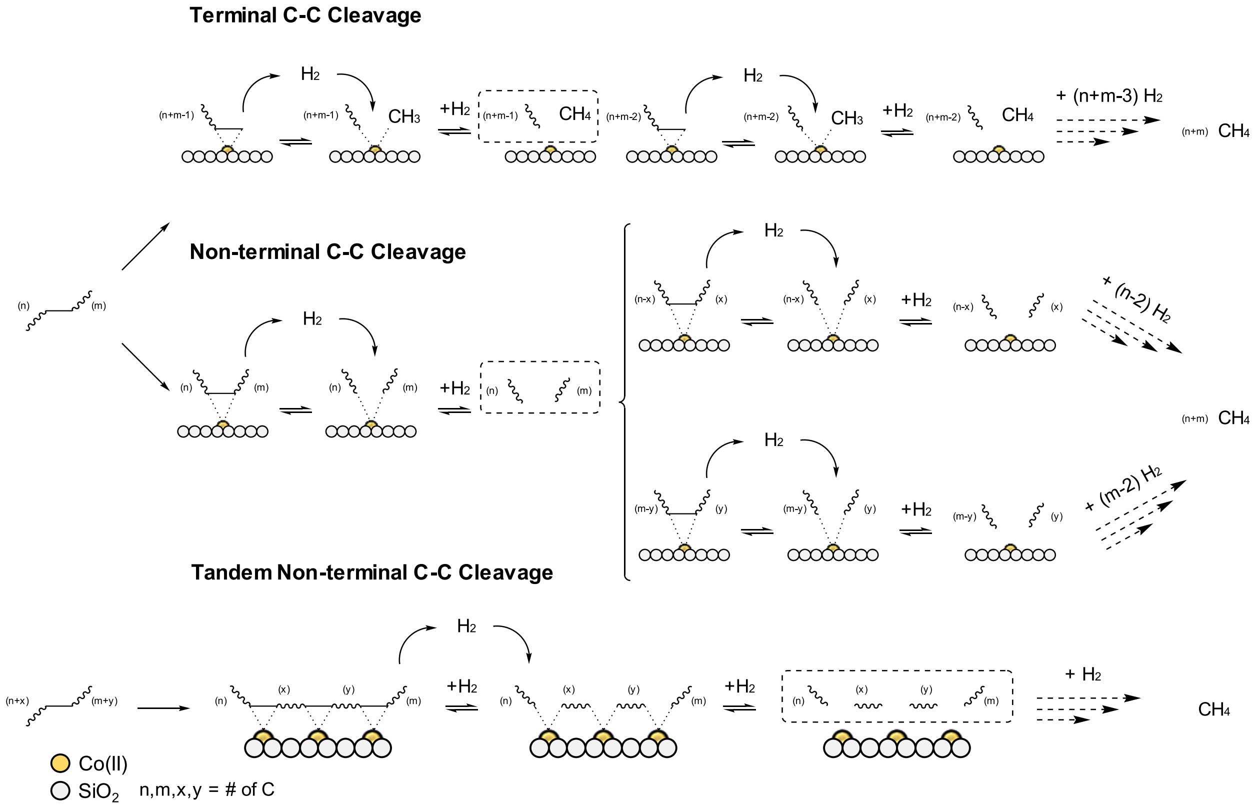

Figure 5. Parallel cleavage routes of PE hydrogenolysis. PE hydrogenolysis can take three parallel routes: (i) terminal C−C cleavage, wherein methane and a PE chain with one carbon less are first formed, followed by the sequential degradation of the PE and an accompanied rise in methane, and eventual conversion to methane, (ii) nonterminal C−C cleavage, wherein two random oligomeric hydrocarbons are first formed, followed by hydrogenolysis of the daughter hydrocarbons to form lower alkanes, eventually forming methane, and (iii) tandem nonterminal C−C cleavage, wherein the PE chain adsorbs onto several active metal sites and cleaves into several daughter oligomeric hydrocarbons, which then undergo further hydrogenolysis, eventually forming methane.

would not dominate until later in the reaction when polymer chains have been cleaved to the liquid range.

The terminal and nonterminal cleavage routes assume that hydrogenolysis occurs as discrete events with only one C−C bond cleaving at a given time. However, it is also possible for several C−C bonds to cleave simultaneously, especially considering the SiO_2 adsorbs the polymer chain in between active metal sites. As such, we propose a third route of *tandem nonterminal* cleavage, as shown in Figure 5, with multiple quasi-simultaneous C−C bond cleavages. Due to the long structure of the polyolefin chain, it is likely that if one internal C−C bond meets the catalyst surface, several nearby points on the chain will likely adsorb to the surface. More specifically, the bonding angle of the sp^3 bonds in the backbone and this intrinsic steric limitation imply that the polymer chain will not form a sharp kink wherein only one C−C bond adsorbs and the adjoining chain segments avoid the surface.[13,42] The chain dehydrogenates, cleaves, and ultimately desorbs from these metal sites. The scission at these sites need not happen synchronously, but rather the proximity of the active sites will result in oligomer-length segments that produce hydrocarbons likely in the lower carbon number (e.g., C_2−C_{30}) range once released. These hydrocarbons could undergo further hydrogenolysis in later events, eventually forming CH_4.

In the tandem nonterminal cleavage route, before multiple successive events occur, the yield of liquid-range or oligomeric hydrocarbons would be likely greater than that of light gases, particularly CH_4. The time series above (Figure 4) suggests that the degree of terminal C−C bond hydrogenolysis is lower than that of nonterminal cleavage on Co/SiO_2 catalysts. This is seen in the higher liquid selectivity at lower conversions (and early reaction times) as oligomers form first and then degrade to gases. The broad liquid distribution and the stable average total carbon number for the first 4 h (Figure 4b and 4e) further support our hypothesis that these oligomers are steadily produced initially. The steady increase in C_2−C_5 gases indicates tandem nonterminal C−C cleavage events and their eventual conversion into CH_4 in later terminal scission events. All routes likely proceed in parallel, but the near-zero CH_4 yields at low reaction times further suggest that terminal C−C cleavage is a minor route (Figure 4c). For the current discussion, the "dominance" of a given cleavage route herein refers to the numerical prevalence and does not refer to reaction kinetics, as a kinetic study is outside the scope of the current work due to mass transfer limitations.

We postulate that the reason for the dominant, tandem, nonterminal cleavage route rests on three underlying principles: alkane adsorption to the Co sites, alkane adsorption to the silica support, and the stochastic preference for internal bonds. Storsæter et al. studied the adsorption of alkanes on a Co/Al_2O_3 Fischer−Tropsch catalyst, finding that alkane chain ends (CH_3−CH_2) have intermediate-strength adsorption enthalpy to the cobalt sites while internal alkane bonds (CH_2−CH_2) show a weak adsorption enthalpy.[43] In line with the established Sabatier principle, intermediate-strength bonds are often favorable for surface reactions, adsorbing strong

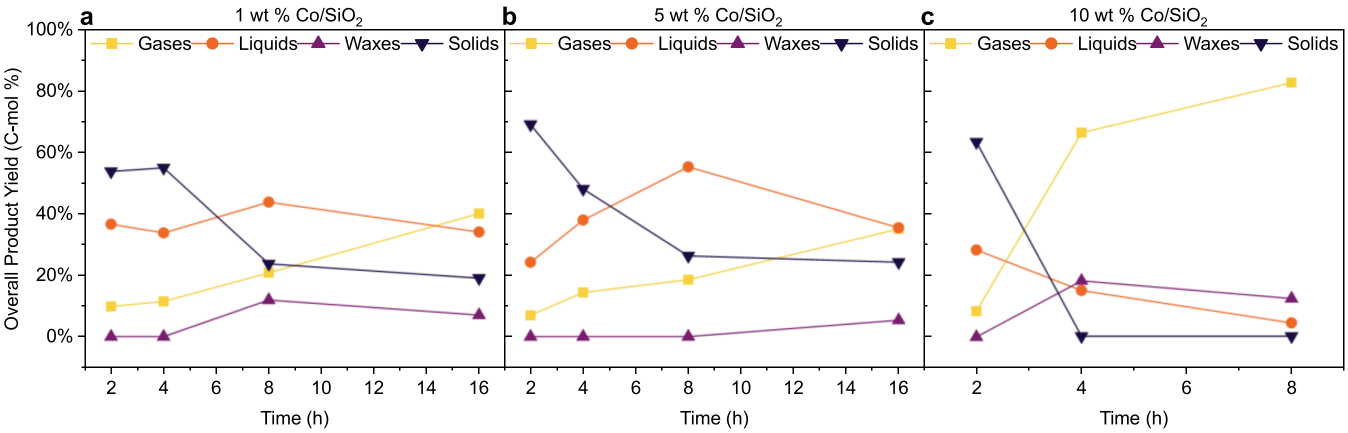

Figure 6. Effect of active metal loading on PE hydrogenolysis over Co/SiO_2. Overall product yield (C-mol %) over (a) 1 wt % Co/SiO_2, (b) 5 wt % Co/SiO_2, and (c) 10 wt % Co/SiO_2. Reaction conditions: 275 °C, 30 bar initial H_2, 2–16 h, 200 rpm, 1.0 g of PE, and 0.5 g of 1 wt % Co/SiO_2, 0.1 g of 5 wt % Co/SiO_2, or 0.05 g of 10 wt % Co/SiO_2.

enough to allow the reaction to occur without strong hindrance to postreaction desorption.[44] As such, the reaction rates for the terminal cleavage route may indeed be higher than those for internal cleavage, although further exploration is needed to unravel the reaction mechanisms and kinetics.

However, this preference for terminal cleavage at the Co site appears to be overshadowed by other driving forces. Various researchers have alluded to the preferential adsorption of longer chains on silica- and alumina-supported catalysts.[45,46] Bhadra et al. investigated *n*-alkane adsorption on hydrophilic and hydrophobic supports, concluding that the increasing dielectric constant of *n*-alkanes with increasing chain length drives adsorption for mesoporous supports.[47] Hydrophobic materials prefer nonpolar adsorbates (shorter chain alkanes), but hydrophilic supports like silica prefer the increased polarity of longer chain adsorbates, as evidenced by their higher dielectric constants.[48] In addition to the support's preference for longer chain alkanes, the shear numerical dominance of internal bonds to terminal dominance (calculated for the model PE used in this study as 283 internal bonds for every 2 terminal bonds, on average) stochastically drives the prevalence of internal bond adsorption over terminal bonds at the beginning of the reaction. We postulate that the first step of the hydrogenolysis reaction mechanism, dehydrogenative adsorption of the C−C bond on the metal, occurs randomly at different locations along the PE backbone, producing a slew of oligomeric hydrocarbons. As the reaction proceeds, the concentration of internal bonds decreases as shorter oligomers are produced, eventually reaching a point (around 16 h) where the stochastic preference swings to support the terminal mechanism as the production of liquids and C_2−C_5 gases declines and methane continues increasing monotonously, as seen in Figure 4.

To investigate these cleavage routes further, in addition to the 5 wt % catalyst, 1 and 10 wt % catalysts (herein referred to as 1-Co/SiO_2, 5-Co/SiO_2, and 10-Co/SiO_2) were synthesized and employed in the reaction at 275 °C and 30 bar initial H_2. The ratio of polymer substrate to active metal (Co) was kept constant, meaning only the average active site density (Co atoms/nm^2 catalyst) and the total catalyst mass varied. Figure 6 shows the product distributions of PE hydrogenolysis, comparing these loadings over the reaction's first 16 h (8 h for 10-Co/SiO_2).

At 2 h, where the solid conversion was low, the three loadings gave similar product yields. Specifically, liquid product yields were 37%, 24%, and 28% while gaseous product yields were 10%, 7%, and 8% for 1-, 5-, and 10-Co/SiO_2, respectively. At 4 h, while 1- and 5-Co/SiO_2 had only slightly greater conversion than at 2 h (in line with the earlier presented time series), 10-Co/SiO_2 converted all of the substrate into majorly gaseous products. At a longer time of 8 h, liquids were the dominant product in 1- and 5-Co/SiO_2 while 10-Co/SiO_2 predominantly produced gases. Further, it was observed that for both 1- and 5-Co/SiO_2, the nongaseous products peaked in their yield at 8 h. We can see further differences between low (≤5 wt %) and high (>5 wt %) catalyst loadings when comparing the evolution of average product carbon over time (Figure S5).

These observations substantiate our hypothesis of nonterminal C−C bond cleavages over Co/SiO_2, albeit with a nuanced balance between active site proximity and particle size. The actual dispersion of cobalt particles on the support is a complex system of varying interparticle distances, particle sizes, and active site densities, as shown via scanning electron microscopy-back-scattered electron (SEM-BSE) imaging shown in Figures S14−S17. The calculated average surface metal density from the synthesized batches increased from 0.24 (1 wt % loading) to 2.19 Co atom/nm^2 catalyst (10 wt % loading) (see Table S21). The SEM-BSE micrographs (see the Experimental Section) reveal that the average cobalt particle size concomitantly *increased* by 67% (from 51.9 to 86.8 nm), the average number of particles per catalyst area *decreased* by 43%, and the interparticle spacing *increased* by 32% (see Figure S18 and Table S22) from 5-Co/SiO_2 to 10-Co/SiO_2.

With increased loadings, the Co particles begin to agglomerate, forming larger, more dispersed particles (Figures S14−S17). We postulate that at low loadings, the Co particles being more distant from each other may undermine the formation of liquid-phase oligomer products. With increased loading, the formation of liquid-phase oligomeric products is enhanced as the interparticle distance reduces up to a certain threshold value. However, once the Co particles grow sufficiently large to allow the polymer to adsorb at multiple locations on the same particle, gas-product formation is enhanced. This may include terminal and internal bonds cleaving in a tandem manner (as discussed above) but producing predominantly gaseous products due to the high

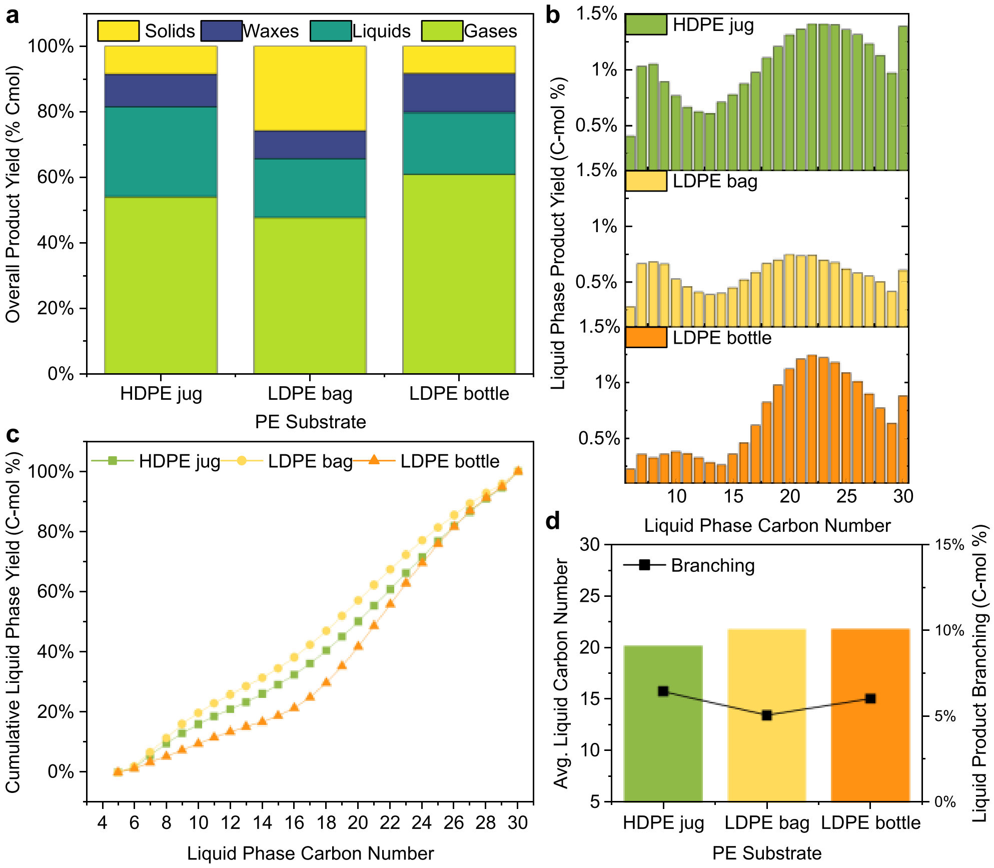

Figure 7. End-of-use plastic hydrogenolysis over Co/SiO_2. (a) Overall product yield (C-mol %), (b) liquid-phase product yield (C-mol %), (c) cumulative liquid-phase product yield (C-mol %), and (d) average liquid-phase product carbon number and liquid-phase product branching (C-mol %) for end-of-use polyethylene substrates including an HDPE jug, a LDPE bag, and a LDPE bottle. Reaction conditions: 275 °C, 30 bar initial H_2, 8 h, 200 rpm, 1.0 g of substrate, and 0.1 g of Co/SiO_2.

proximity of adsorption sites. Conversely, below the threshold loading, metal particles likely have a similar surface density (particles/nm^2), with particle size predominantly changing with metal loading, resulting in similar products due to the tandem, nonterminal cleavage mechanism.

It has recently been shown that bulk Co_3O_4 favors terminal C−C bond cleavage in PE hydrogenolysis, producing predominantly methane.[37] We postulate that a bulk Co_3O_4 catalyst demonstrates terminal cleavage events as this emulates a limiting case of high wt % metal loading (with no support dispersing the Co), similar to the 10 wt % loading. To probe this, we replicated a high-conversion reaction (16 h, 30 bar initial H_2, and 275 °C) with bulk Co_3O_4 (BET surface area of 18 m^2/g), producing almost exclusively methane (Table S10), compared to the range of alkanes produced by the silica-supported catalyst (see Figure 4). We then compared Co_3O_4 to Co/SiO_2 at intermediate conversion (4 h, 30 bar initial H_2, and 275 °C), maintaining the same active metal-to-polymer substrate ratio as the Co/SiO_2 reactions above, i.e., using 5 mg of bulk Co_3O_4. A similar solid residue was seen with a much higher wax yield than Co/SiO_2, suggesting a lower degree of conversion. The bulk cobalt oxide seems to act similarly to the 10-Co/SiO_2, which has large, highly dispersed metal particles. Large agglomerations of Co_3O_4 increase the strength of C−C bond adsorption of terminal and proximity C−C bonds, facilitating cleavage to lower gaseous alkanes (especially methane) early in the reaction. On the other hand, dispersed cobalt oxide sites on a redox-inert support allow for a range of oligomeric products. The polymer chain weakly adsorbs to the redox-inert support between metal sites. Thus, it allows quick desorption of the cleaved branches, preventing cascading terminal scission and producing liquid products from the initial events.

Next, the applicability of the catalyst to hydrogenolysis of postconsumer waste polyethylenes was tested on end-of-use plastics: HDPE (VWR solvent jug) and LDPE (packaging bag and solvent bottle). HDPE and LDPE differ primarily in the linearity of the hydrocarbon backbone and crystallinity.[49] As these substrates were used without purification or pretreatment, they were assumed to have varying impurities, fillers, molecular masses, branching, and crystal structure.[42] Figure 7a and 7b shows three different PE substrates yielded similar overall and liquid-phase product yields and distributions. Specifically, the solid, liquid, and gas yields ranged between 8% and 26%, 18% and 27%, and 48% and 61% for the three PEs. The average liquid-phase carbon numbers for all PE substrates fell in a narrow range of C_{20}−C_{22} (Figure 7d). Interestingly, it was also observed that the liquid products show a bimodal distribution. This is characteristic of high-conversion PE hydrogenolysis with comparable yields of liquid and gaseous products (see Figures 2−4) as lower alkanes are rapidly formed from the hydrogenolysis of daughter polymer chains. Hydrogenolysis of a polypropylene (PP) substrate (fruit cup) was also tested under identical conditions (Table S11). The consistency of these results shows this catalyst's effectiveness and flexibility to various macromolecular polyethylene

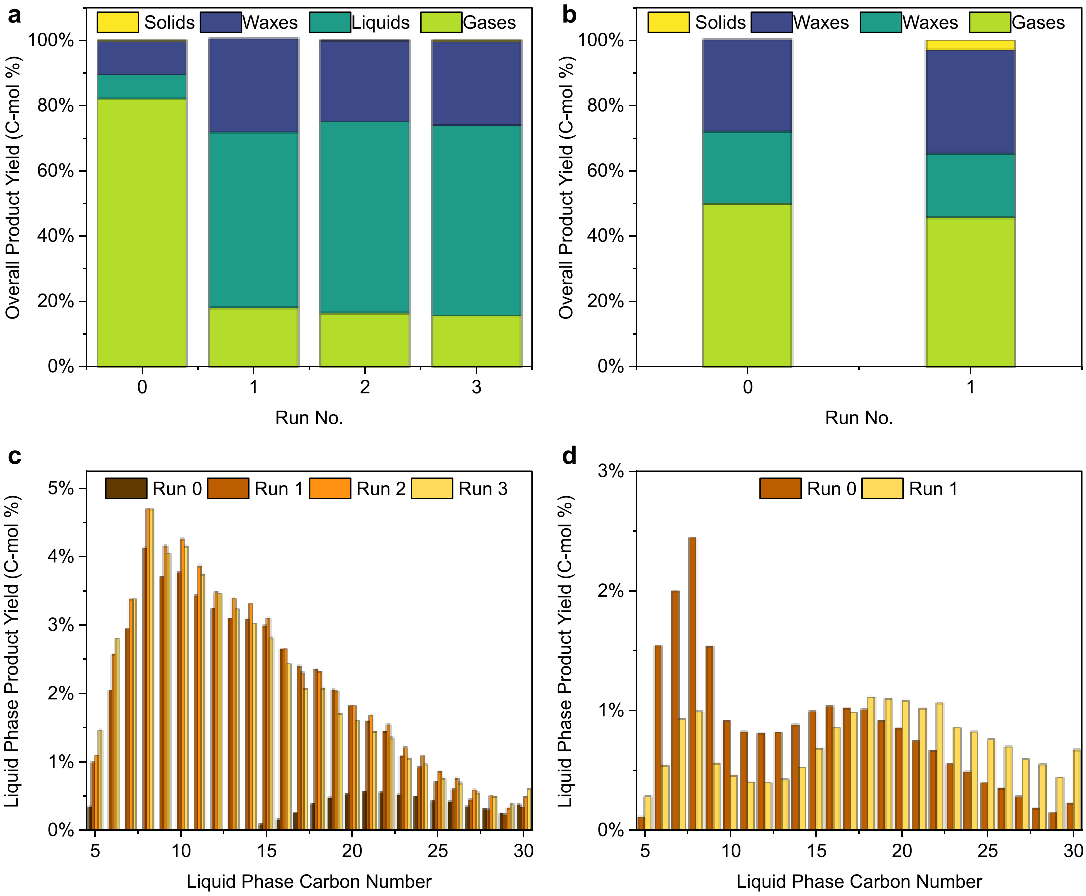

Figure 8. Recyclability of Co/SiO_2 catalyst in PE hydrogenolysis. Overall product yield (C-mol %) of (a) catalyst reuse runs and (b) catalyst regeneration runs, and liquid-phase product yield (mg) of (c) catalyst reuse runs and (d) catalyst regeneration runs. Reaction conditions: 300 °C, 30 bar initial H_2, 4 h, 200 rpm, 1.0 g of substrate in all reuse runs and regeneration run 0, and ~0.55 g of substrate in regeneration run 1, 0.1 g of Co/SiO_2 in both runs 0 and all recovered catalyst in subsequent runs.

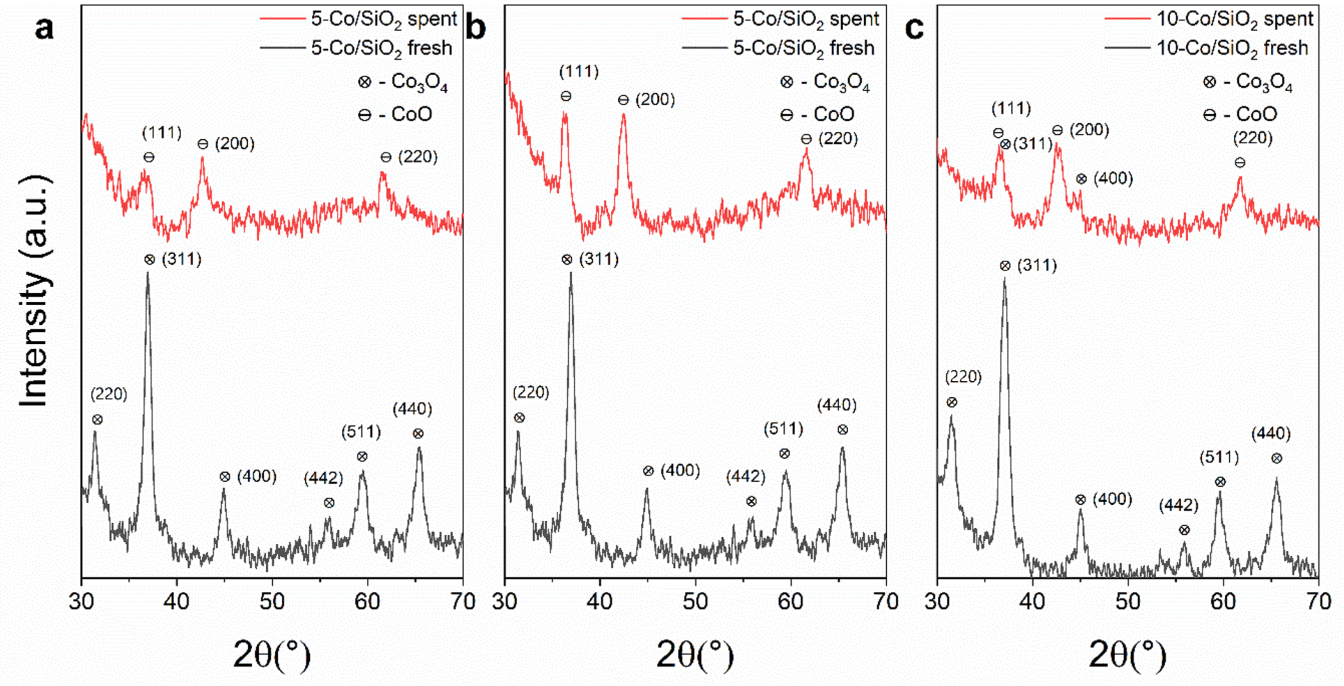

Figure 9. Pre- and postreaction powder X-ray diffraction patterns of Co/SiO_2. Reaction conditions: (a) 275 °C, 30 bar initial H_2, 16 h, 200 rpm, 1.0 g of PE, and 0.1 g of 5-Co/SiO_2, (b) 300 °C, 30 bar initial H_2, 4 h, 200 rpm, 1.0 g of PE, and 0.1 g of 5-Co/SiO_2, and (c) 275 °C, 30 bar initial H_2, 8 h, 200 rpm, 1.0 g of PE, and 0.05 g of 10-Co/SiO_2.

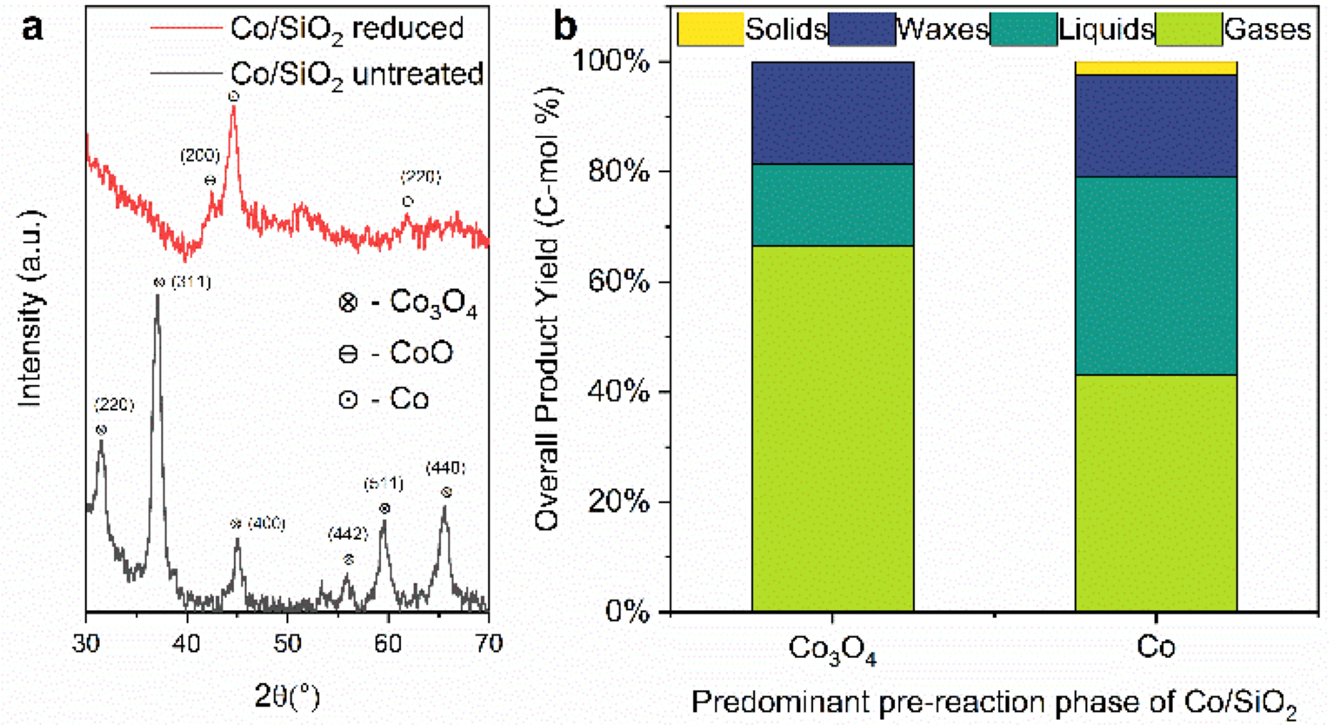

Figure 10. Catalytic performance of pretreated Co/SiO$_2$ in PE hydrogenolysis. (a) Powder X-ray diffraction patterns of untreated and reduced 10 wt % Co/SiO$_2$ catalyst samples. (b) Overall product yield of PE hydrogenolysis over untreated and reduced Co/SiO$_2$ catalysts with dominant prereaction phase Co$_3$O$_4$ and Co, respectively. Reaction conditions: 275 °C, 30 bar initial H$_2$, 4 h, 200 rpm, 1.0 g of substrate, and 0.05 g of 10 wt % Co/SiO$_2$.

architectures, despite the variabilities in the properties of the PE substrates.

Next, we investigated the reusability and regenerability of the catalyst. These were tested first by reusing the catalyst without any treatment between runs. These reactions were carried out at 300 °C, 30 bar H$_2$ for 4 h to maximize the solid conversion and enable the easy extraction of the catalyst postreaction. It was assumed that the postreaction solids were predominantly catalysts. The solids were directly added to the subsequent run to test the catalyst's direct reuse, while the PE substrate mass was kept the same (1.0 g). It must be noted that there was about a 10% catalyst mass loss between each run. Figure 8a shows that largely gaseous hydrocarbons (~82% yield) were produced using the virgin catalyst. The catalyst was reused 3 more times. During the first reuse, the liquid products were favored with ~54% yields with ~18% and ~29% gas and wax yields, respectively, with little change in each subsequent run.

Alternatively, to evaluate the catalyst's recyclability, the postreaction catalyst was calcined at 450 °C for 5 h under air and subsequently contacted with PE under identical reaction conditions, maintaining the catalyst-to-substrate ratio at 1:10. The regenerated catalyst produced a similar product distribution as compared to the virgin catalyst with less than 5% variation in each of the gas, liquid, wax, and solid yield (Figure 8b). These two comparative studies showed that the hydrogenolysis activity of Co/SiO$_2$ decreased when reused without treatment, which can be attributed to either catalyst deactivation through carbon deposition or an in situ change in the metal phase (due to the high-temperature reductive environment) leading to an inherent change in catalyst activity. This change is, however, reversible, and the catalyst's activity can be restored by postreaction calcination. Further, our observations suggest that the change in activity is not progressive either, meaning that after the first run, the catalyst can be reused several times to give a similar product distribution. The mass balances, liner mass balances, and product phase distributions for all studies are tabulated in the SI in Tables S3−S14.

The cause of the change in product distribution in reuse data (Figure 8) and possible catalyst deactivation was investigated first by identifying the cobalt phase postreaction using PXRD. Specifically, the phase of catalyst pre- and postreaction was probed via PXRD for two runs using the 5 wt % Co/SiO$_2$ (5-Co/SiO$_2$: 275 °C and 16 h and 300 °C and 4 h) and another using 10 wt % Co/SiO$_2$ (10-Co/SiO$_2$: 275 °C and 8 h) (Figure 9).

First, the prereaction catalyst showed diffraction patterns corresponding to Co$_3$O$_4$ for both metal loadings.[50,51] All spent catalyst samples recovered postreaction (both 275 and 300 °C) showed peaks at 2θ values corresponding to lattice planes of CoO,[50] confirming that the catalyst underwent partial reduction during the reaction. The peak locations in the spent catalyst samples across various reaction conditions (temperature and time) were similar, suggesting that the catalyst did not undergo any significant phase change after being partially reduced in situ, explaining the uniform activity in the reuse runs. Due to the limited postreaction catalyst amount and the presence of residual crystalline PE, the signal-to-noise ratio of the PXRD patterns was reduced. However, the peak locations helped identify the catalyst phase postreaction. These findings reveal that the catalyst reduces from Co$_3$O$_4$ to CoO under the reaction conditions and remains in that phase without oxidative regeneration. On recalcination of the spent catalyst, the Co$_3$O$_4$ phase is regenerated (Figure S6), along with the probable removal of any residual species deposited on the catalyst. This treatment restored the catalyst's activity, as was observed in the recycle run with postreaction calcination (Figure 8b). Therefore, it is postulated that calcination reactivates the catalyst by primarily removing recalcitrant polymer species from the surface. As the PXRD patterns are similar for the spent catalyst samples, both singly used and reused (Figure 9), the phase change is likely not the cause of the change in product yields after the first reaction in the reuse study (Figure 8a), as it appears to remain constant after partial reduction under reaction conditions. Conversely, PXRD analysis of the pre- and postreaction bulk Co_3O_4 catalyst showed a complete reduction to cobalt metal (Co(0)) under the reaction conditions (Figure S7). This aligns with the recent study by Román-Leshkov and co-workers, who showed that while bulk Co_3O_4 was reduced to pure Co, Co/ZSM-5 did not reduce due to lattice oxygen supplied by the support material, highlighting that the SiO_2 support hinders the reduction of cobalt oxide.[37]

To isolate the impact of phase change on the catalytic activity and selectivity, we pretreated 10-Co/SiO_2 (600 °C, 4 h, 33% H_2 in N_2, total flow 50 mL/min) before the reaction, which reduced the Co_3O_4 to predominantly Co.[50] PXRD patterns confirming these phases are shown in Figure 10a. The prereduced catalyst (predominantly Co) showed only a minor change in product selectivity, as shown in Figure 10b. Specifically, the product yield in the gas phase dropped from 66% to 43%, while that in the liquid phase increased from 15% to 36%. The solid residues were 0% and 2%, respectively. The detailed mass balances of these runs are given in Table S14. These findings reinforce our hypothesis that in situ reduction of the Co/SiO_2 did not significantly affect the activity and that coking was the dominant reason for the activity change.

After investigating the impact of the metal phase, we tested for the presence of carbonaceous species via thermogravimetric analysis (TGA) of the postreaction catalysts coupled with evolved gas analysis via mass spectrometry (MS) for carbon dioxide evolution. Specifically, postreaction catalyst samples were taken from three exemplary high-conversion reactions, namely, (a) 4 h, 40 bar H_2, 275 °C, (b) 36 h, 30 bar H_2, 275 °C, and (c) 4× repeated runs of 4 h, 30 bar H_2, 300 °C each. To deconvolute the release of carbonaceous coke from polymeric species, a TGA program was implemented based on methods applied to biomass fraction determination,[52] including a temperature-programmed pyrolysis (TPP) stage to 600 °C followed by cooling in an inert atmosphere and temperature-programmed oxidation (TPO) to 650 °C after that. Polyethylene has been shown to pyrolyze under an inert atmosphere by 550 °C.[53] At the same time, carbonaceous coke does not appreciably release in an inert atmosphere below 600 °C.[54] Conversely, in air, coke is shown to release at temperatures below 650 °C,[54−56] which was confirmed by tests with pure PE substrate and activated carbon (Figures S8−S10).

The TPP testing of the three samples showed a significant portion of recalcitrant polymer remaining on the catalyst, ranging from 10.5 to 18.5 wt % (Table S19 and Figure S12). At the same time, the TGA-MS data revealed negligible CO_2 or coke formation and solid mass loss (<0.1 wt %) during the oxidation phase (Figure S11 and Table S20). As our tests demonstrated that graphitic coke, chemically similar to activated carbon,[55] would oxidize by 650 °C (Figure S9), these results indicate that a "hard" coke species was not formed to a significant extent during the hydrogenolysis reactions. However, the significant presence of the pyrolyzed species in all of the high-conversion samples in Table S19 revealed that a portion of the substrate integrates with the catalyst to become recalcitrant to the hydrogenolysis reaction conditions. Therefore, although the precise mechanism of its resistance to hydrogenolysis is unknown, we postulate that the shift in catalytic selectivity after one reaction results from the formation of resistant, polymeric hydrocarbon species, structurally like PE, rather than a carbonaceous coke.

To understand the changes in catalyst structure from this species, the BET surface area was measured from N_2 physisorption on a single-spent, high-conversion catalyst sample (4 h, 30 bar H_2, 300 °C), applying similar successive pyrolysis (600 °C) and oxidative calcination (450 °C) (Table 1). Compared to fresh catalyst (not used in PE hydrogenolysis), spent catalyst experiences a sharp decline in surface area from 320 to 209 m^2/g, which is mostly recovered after pyrolysis, reaching 291 m^2/g. Furthermore, the increase in average pore diameter may result from smaller macropores being obstructed by the recalcitrant polymer. The oxidative calcination shows a further increase in surface area to 390 m^2/g. This is likely due to structural changes in the silica support. This increase in surface are can be augmented up to 500 °C and then reduced above 500 °C.[57] In line with the findings from the TGA-MS, we postulate that a portion of the polymer substrate forms a recalcitrant species around the catalyst, blocking access of fresh substrate to the active sites. In line with the tandem, nonterminal cleavage mechanism, successive scission events will be reduced with fewer accessible active sites, and the average distance between accessible sites would also increase, thus resulting in longer oligomer products.

Table 1. BET Surface Area, Pore Volume, and Average Pore Diameter from N_2 Physisorption of Pre- and Postreaction Heat-Treated 5 wt % Co/SiO_2 Samples[a]

catalyst condition	BET surface area (m^2/g)[b]	pore volume (cc/g)	average pore diameter (nm)
prereaction	320 ± 6	1.578	19.67
postreaction	208 ± 5	1.246	23.87
postreaction, pyrolyzed (600 °C)	291 ± 17	1.426	19.55
postreaction, pyrolyzed (600 °C) and calcined (450 °C)	390 ± 40	1.929	19.77

[a] Reaction conditions: 300 °C, 30 bar initial H_2, 4 h, 200 rpm, 1.0 g of PE, and 0.1 g of 5 wt % Co/SiO_2. Complete isotherms are shown in Figure S13. [b] The errors in the BET surface area have been calculated with reference to a least count error of 1.0 mg of the balance.

■ CONCLUSION

Overall, we showed silica-supported cobalt (Co/SiO_2) to be a promising alternative to the rare-earth Ru/SiO_2 for polyethylene (PE) hydrogenolysis under mild reaction conditions of 200−300 °C and 20−40 bar H_2. Crucially, we optimized the reaction parameters (temperature, initial pressure, and reaction time) to direct the selectivity toward desired hydrocarbon products on the Co/SiO_2 catalyst. At 275 °C and 30 bar H_2 for 8 h, liquid yields were optimized to selectively produce ∼55% liquids and ∼19% gases, respectively, with an average liquid C_n = 21.8 from a model PE substrate of M_w = 4000 g/mol.

To achieve optimal catalytic performance, we investigated the reaction pathways of PE hydrogenolysis. The product yields with varying reaction times and catalyst (i.e., Co) loadings (or Co surface density) demonstrated a catalytic preference toward nonterminal C−C bond cleavage over terminal cleavage. The analysis of metal particle size and surface density revealed the importance of the adsorption strength and proximity along the polymer chain, coupled with a stochastic preference for C−C cleavage, to yield liquid-range products on the supported catalyst.

The catalyst also showed recyclability over four reactions with reduced activity and a shift in yield toward liquid products after the first reaction. Specifically, the selectivity shifted from predominantly gaseous to majorly liquid products (7% vs 53% liquid-phase selectivity). Subsequent catalyst reuse showed no further change in activity or selectivity. The catalyst showed excellent recyclability with the catalyst reactivity recovered on calcination under air at 450 °C, yielding an identical product distribution as the fresh catalyst.

Postreaction powder X-ray diffraction (PXRD) patterns and thermogravimetric analysis coupled with mass spectrometry of the exhaust gases (TGA-MS) together revealed the influence of catalyst phase on the product yields and selectivity and the catalyst deactivation mechanisms. Postreaction PXRD revealed that Co/SiO_2 reduced from Co_3O_4 to CoO during the reaction. Pretreatment of the catalyst to Co shifted the selectivity from gases to liquids by only ∼20%, highlighting that a change in the phase is only a minor contributor to a change in catalyst activity.

TGA-MS revealed negligible hard, graphitic coke deposition on postreaction catalysts and highlighted the presence of a recalcitrant polymeric hydrocarbon species remaining on the catalyst after the reaction. N_2 physisorption of postreaction catalysts confirmed that this recalcitrant polymer reduced the surface area of the catalyst, blocking access of the substrate to active sites on the catalyst.

The catalyst was effective in the conversion of postconsumer PE (HDPE jug, LDPE bag, and LDPE bottle) into liquid and gaseous hydrocarbons, showing its effectiveness toward the hydrogenolysis of PEs with impurities, fillers, and additives in the substrates. Kinetic studies and further investigation into metal loading, particle size, and the type of support for cobalt catalysts could shed further light on the regioselectivity, support, and particle size effects toward nonterminal C−C cleavage of the hydrogenolysis reaction mechanism.

■ EXPERIMENTAL SECTION

Materials. Cobalt(II) nitrate hexahydrate (ACS reagent, 98%, Sigma-Aldrich), iron(II) nitrate nonahydrate (ACS reagent, 98%, Sigma-Aldrich), ruthenium(III) nitrosyl nitrate in dilute nitric acid (Sigma-Aldrich), palladium(II) nitrate dihydrate (40% Pd basis, Sigma-Aldrich), and tetraamine platinum(II) nitrate (99.995%, Sigma-Aldrich) precursors were used to synthesize the supported catalysts. The support, silica (fumed), was purchased from Sigma-Aldrich. Pentane (reagent grade, Ward's Science) and hexane (ReagentPlus, 99%, Sigma-Aldrich) were used for GC product identification, and octadecane (99%, Sigma-Aldrich) was used as a model compound. Benzene (HPLC grade, 99.9%, Sigma-Aldrich) was used as the internal standard for liquid-phase product calibration. Ethyl acetate (ACS grade, 99.5%, VWR) was used as a solvent for liquid product extraction. Polyethylene (average $M_w \approx 4000$, Sigma-Aldrich) was used as the primary substrate in the study, while HDPE (VWR solvent jug), LDPE (packaging bag and VWR solvent bottle), and PP (fruit cups) were directly used after cutting them into ∼3−4 mm square pieces. Activated carbon (Darco G-60, −100 mesh, Sigma-Aldrich) was used as reference material for thermogravimetric analysis. All commercially obtained chemicals were used without further purification.

Catalyst Synthesis. Catalysts were prepared using the incipient wetness impregnation method. Unless otherwise stated, all catalysts were synthesized with calculations to target a 5% mass fraction of the natural oxidation state of the metal on the catalyst support (i.e., Co_3O_4, Fe_2O_3, PdO, Pt, and RuO_2) at room temperature. To synthesize the Co catalyst, in brief, for 2.5 g of supported cobalt oxide catalyst, 0.9 g of cobalt(II) nitrate hexahydrate was dissolved in ∼5 mL of distilled (DI) water (18.2 MΩ, Thermo Scientific Barnstead Smart2Pure Water Purification System UV/UF). The masses of the precursors were adjusted for other metals and different loadings. The precursor solution was then added dropwise to 2.375 g of SiO_2 support, followed by vigorous stirring and dispersing agglomerates using a metal spatula to disperse the metal onto the support evenly. The catalyst was next transferred to a ceramic crucible and placed uncovered in a muffle furnace at 120 °C (ramp rate of 5 °C/min) for 12 h in a flow of air at 50 mL/min and then calcined at 450 °C for 5 h (ramp rate of ∼4 °C/min) at the same air flow rate of 50 mL/min before allowing it to cool to room temperature. The catalysts were stored in a desiccator and used for reactions without further pretreatment unless otherwise stated.

Catalyst Characterization. All prereaction characterization was carried out on calcined samples. Postreaction characterization of the catalysts was carried out after drying the postreaction samples in a convection oven in air at 100 °C for 12 h. Powder X-ray diffraction (PXRD) patterns were collected with a Rigaku Miniflex II X-ray with Cu Kα radiation (λ = 1.5406 Å) from 5° to 75° at a step rate of 0.02 and scan rate of 1°/min. The diffraction patterns were baseline corrected using Match!, Version 3.15, and smoothened using 10-point window adjacent averaging on OriginPro, Version 2023. Surface area measurements were conducted on an Anton Paar Autosorb iQ-C-MP EPDM automated gas sorption analyzer. The surface area was determined using nitrogen physisorption (at 77 K) and analyzing adsorption−desorption isotherms using Brunauer−Emmett−Teller (BET) theory.[58] In brief, 10−150 mg of the catalyst sample was loaded in a 6 mm glass cell bulb (without a rod). The sample was first outgassed at 350 °C for 480 min. Nitrogen physisorption isotherms were measured using 40 adsorption/desorption points with p/p_o values ranging from 0.025 to 0.995. BET analysis was performed on the isotherm data using adsorption data points of p/p_o from 0.05 to 0.35. Pore volume and average pore diameter calculations were based on assumptions of a macroporous structure with cylindrical pore geometry due to the type IV isotherm with type H1 hysteresis observed, assuming the pores are filled with liquid adsorbate at relative pressures close to unity, as shown below[59]

$$V_{\text{liq}} = \frac{P_a V_{\text{ads}} V_m}{RT} \tag{1}$$

where P_a is ambient pressure, T is ambient temperature, V_m is the molar volume of liquid adsorbate (nitrogen), V_{liq} is the volume of liquid adsorbate in the pores, and V_{ads} is the volume of adsorbate absorbed to the surface.

The average pore radius r_p was calculated assuming a cylindrical port geometry (based on type H1 hysteresis), as shown below, using BET surface area S

$$r_p = \frac{P_a V_{\text{ads}} V_m}{RT} \tag{2}$$

Scanning Electron Microscopy Imaging. A Tescan FERA-3 model GMH Focused Ion Beam Microscope (FERA FIB-SEM, RRID:SCR_022202) was used to procure scanning electron microscopy-back-scattered electron imaging on various catalysts, including 10, 5, and 1 wt % Co/SiO_2, in addition to nonloaded silica. Exemplary images are shown in Figures S14-S17. The 1 wt % catalyst did not display catalyst particles visible to SEM-BSE, appearing similar to the pure SiO_2 sample, and is thus not shown for brevity's sake. Image analysis to quantify changes in cobalt particles on the support was applied using Paint.NET Digital Photo Editing software, uniformly applying the following procedure to both the 5 and the 10 wt % sample micrographs of near identical parameters (see Figure S18).

(1) The Highlights/Shadows tool was used to enunciate the catalyst particle "highlights" in the image.
    (a) First pass settings: highlights, +100; shadows, −100; clarity, 100; radius, 10.00.
    (b) Second pass settings: highlights, 0; shadows, −100; clarity, 100; radius, 10.00.
    (c) Third pass settings: highlights, −50; shadows, −100; clarity, 100; radius, 5.00.
    (d) Fourth pass settings: highlights, −50; shadows, −100; clarity, 100; radius, 1.25.
    (e) Fifth pass settings: highlights, −100; shadows, −100; clarity, 100; radius, 1.25.

(2) The Levels Adjustment tool was used to increase contrast, making catalyst areas white and other areas almost black.
    (a) Settings: Input from 0 to 125. Output from 0 to 255 with 7.99 median. R, G, and B channels selected.

(3) The Noise Median effect was used to filter out small white spots that were not indeed catalyst areas, produced in the above two steps.
    (a) Settings: radius, 1; percentile, 50.

(4) The Magic Wand tool (set to a Global flood, 75% tolerance) was used to select catalyst areas, clicking on a pure white spot.
    (a. The selected area was sent to a new layer and filled with black for quantification.

(5) The remaining catalyst areas and total analysis area were analyzed as follows (see Table S22 for results).
    (a) The catalyst area (black objects) and total analysis area in terms of pixels were recorded.
    (b) The individual catalyst area objects were counted to quantify the number of catalyst particles.
    (c) The scale bar was measured to convert pixel length to nanometers. The scale bar was of identical size in both pictures.
    (d) (Average) Particle diameter (nm, of Co particles) was calculated as follows, assuming particles appear as square objects.

(d.i)

$$D = \sqrt{\frac{\text{catalyst area (square pixels)}}{\text{number of catalyst objects}}} \times \left(\frac{17.54\ \text{nm}}{\text{pixel}}\right) \quad (3)$$

    (e) (Average) Particle dispersion (Co particles per square micrometer of catalyst surface) was calculated as follows.

(e.i)

$$PD = \frac{\text{number of catalyst objects}}{\text{total analysis area (square pixels)}}\left(\frac{\text{pixel}}{0.01754\ \mu\text{m}}\right)^2 \quad (4)$$

    (f) (Average) Interparticle distance (nanometers between Co particles) was calculated as follows, assuming particles are dispersed on a square grid of the image.

(f.i)

$$ID = \sqrt{\frac{\text{square micrometers}}{PD(\text{particles})}} \times \frac{1000\ \text{nm}}{\mu\text{m}} \quad (5)$$

    (g) Surface coverage (percent of surface covered by Co particles) was calculated as follows.

$$\text{coverage} = \frac{\text{catalyst area (square pixels)}}{\text{total analysis area (square pixels)}} \quad (6)$$

Catalyst Testing. The hydrogenolysis reactions were carried out in a 100 mL stainless-steel Parr reactor equipped with a stainless-steel stirrer, where the catalyst was in contact with polyolefins in the melt phase under reaction conditions (substrate/catalyst ratio of 10, typically 1.0 g of the substrate, and 0.1 g of the catalyst) between 200 and 300 °C (ramp rate of 5−10 °C/min), 10−40 bar H_2, and 2−36 h catalyst contact time (reaction time). All polyethylene reactions were carried out in a borosilicate liner supplied by Parr to create an inert reaction surface, while reactions with n-C_{18} were carried out without the liner at 200 °C. The borosilicate liner was topped with a custom-made concave PTFE liner to seal the annular region between the liner and the reactor vessel. The actual reactor volume was determined to be ∼85 mL by pressurizing the reactor with N_2 to ∼20 bar and then allowing the gas to expand into an evacuated stainless-steel pipe of a known volume (∼58 mL). The volumes, the final pressure of the stainless-steel pipe, and ideal gas law were used to estimate the volume inside the reactor. The reactor was heated using a rigid heating quartz fabric mantle in an aluminum housing and controlled by the Parr 4848 temperature controller. The stirring speed was 200 rpm for PE reactions (100 rpm for octadecane reactions) to ensure optimal mass transfer (see Tables S15 and S16). The stirring speed was selected to achieve optimal catalyst contact and minimize mass transfer limitations. Specifically, very high stirring rates (>400 rpm) caused ineffective catalyst contact, i.e., splashing of the catalyst onto the reactor walls and low conversion. In contrast, no stirring resulted in low conversion due to ineffective mass transfer. Before loading the gas, the substrate and the catalyst were loaded into the liner and shaken until evenly mixed. The liner was placed inside the reactor, followed by the PTFE ring. The reactor was sealed and purged three times with N_2 and three times with H_2 at ∼40 bar and then charged to the initial H_2 pressure (typically 30 bar). The zero time (i.e., $t = 0$) was considered when the reaction temperature was reached. After the specified reaction time, the temperature controller was stopped and the reaction was quenched by dipping the reactor vessel in an ice bath.

Reaction Workup. Once quenched to ∼10 °C using an ice bath, the gaseous products in the headspace of the reactor were captured in a custom gas sampling tube (an ∼58 mL stainless-steel pipe mounted with a pressure gauge) for analysis. The liquid products were mixed with ∼20 mL of ethyl acetate and ∼0.1 g of benzene as an internal standard. The reactor was sealed and heated to 150 °C for 1 h under stirring to dissolve all liquid products in the liner effectively and those trapped in any cold spots in the headspace of the reactor. After cooling to room temperature, the mixture was filtered, and a small aliquot of the liquid was captured in a gas chromatography vial for analysis. The solid residue captured in the filter paper and that left in the liner was dried in an oven at 80 °C and weighed separately. To capture any liquid products that may have condensed in the reactor vessel (outside the borosilicate liner), a second similar liquid extraction was done using another ∼20 mL of ethyl acetate and ∼0.1 g of benzene at 150 °C. The liquids were again filtered, and an aliquot of the liquid was captured.

Product Analysis. A gas chromatography (GC) system equipped with a mass spectrometer (MS) (Agilent 5977C) and a flame ionization detector (FID) (Agilent 8890) was used for the identification and quantification of all products. The gaseous product was injected into the GC system (GS-GasPro 60 m × 320 μm × 0.25 μm column) through a gas sampling valve with a volume saturating the column from the gas sampling tube at least four times for each sample, and the averaged signal was reported. Gas calibrations were performed using known concentrations of methane (CH_4) in H_2. Other gaseous products (ethane, propane, butane, and pentane) were quantified with reference to CH_4 using relative response factors calculated relative to CH_4 according to the enthalpy of the combustion method (tabulated in Tables S17 and S18).[60] The total amount of gas in the reactor was calculated using the ideal gas law and the known volume and pressure of the sample tube.

The liquid products were injected into the GC system (HP-5 30 m × 320 μm × 0.25 μm column) using an autosampler (volume of 2 μL). Product quantification was achieved using an n-octadecane calibration using benzene as an internal standard. The quantities of liquid products (C_5−C_{30}) were calculated using the relative response factor method relative to octadecane according to the enthalpy of the combustion method (tabulated in Table S18).[60] Liquid compounds heavier than C_{30} were lumped together as C_{30+} hydrocarbons, and branched alkanes were identified as those peaks that appeared at residence times lower than the *n*-alkane peak, in line with a recent study by Chen et al.[39] Low boiling liquid alkanes (C_5−C_8) were also observed in the gas phase. C_6 and C_7 were particularly seen in small quantities in low-conversion reactions. These alkanes are liquid at room temperature, so they have been counted only in the liquid phase. C_5 is quantified in both the gaseous and the liquid phases.

The solid residue was determined by subtracting the initial catalyst mass from the total solids remaining in the liner and the filter papers. All conversions, yields, and carbon balances were reported on a carbon mole (C-mol%) basis. The mass balances are confirmed from a total mass balance of the liner minus gas products, which are independently determined from the methods above. This was done to estimate the masses of the nongaseous products and the solid residue (Tables S3−S14). The small masses not captured in the liquid phase or the solid residue were assumed to be C_{30+} waxes. The suspension in the collected liquid sample postextraction with ethyl acetate further visually verified the presence of nominally soluble waxes. The PE hydrogenolysis reaction using 5 wt % Co/SiO_2 at 275 °C and 30 bar for 4 h, used as a central condition across several studies reported herein, was averaged over 4 identical reactions.

The carbon balance of the reaction was calculated according to the following

$$C_{\text{captured}} = \frac{C_g + C_l + C_s}{C_{\text{sub}}} \times 100\% \tag{7}$$

C_{sub} is the initial substrate's amount (in C-mol) and C_g, C_l, C_s, and C_{captured} are the gas, liquid, solid, and total captured products, respectively. The amount of waxes was calculated as

$$C_w = (1 - C_{\text{captured}}) \times 100\% \tag{8}$$

Yield of the *z*th individual carbon number product was calculated as

$$Y_z = \frac{C_z}{C_{\text{sub}}} \times 100\% \tag{9}$$

The yield for pentane (C_5) was summed over the gaseous and liquid phases.

Phase product selectivity (per gas, liquid, and wax phases) was calculated as follows

$$F_{g,l,w} = \frac{C_{g,l,w}}{C_g + C_l + C_w} \times 100\% \tag{10}$$

Catalyst Recycling. Postreaction catalysts were obtained from the solid residue of the previous reaction and charged into the subsequent reaction with identical substrate mass and reaction conditions as the previous run. In another experiment, the postreaction catalyst was regenerated by transferring the solid residue from a previous reaction into a ceramic crucible and calcining the residue at 450 °C for 5 h using a ramp rate of ∼4 °C/min in an air flow of 50 mL/min. The regenerated catalyst was then charged into the reactor with the same catalyst to substrate ratio of 1:10 and identical temperatures, H_2 pressures, and reaction times.

Spent Catalyst Coke Analysis. Thermogravimetric analysis was conducted in a TA Instruments Thermogravimetric Analyzer (TGA) Q5000 IR with an infrared furnace fed with ultrahigh purity nitrogen gas and Ultra-Zero air with 100 μL platinum pans rated to 700 °C. The testing regimen (ramp rates, gas selection, purge flow, sample mass) is explained in the Supporting Information, Figures S8−S10. Drying phase: 10 °C/min ramp to 120 °C followed by a 15 min isothermal phase; 20 mL/min N_2. Temperature programmed pyrolysis (TPP) phase: 30 °C/min ramp to 600 °C, followed by a 5 min isothermal phase. Finally, the sample is cooled to 120 °C; 20 mL/min N_2 during the entire phase. Temperature programmed oxidation (TPO) phase: switch gas from pure N_2 to dry air, followed by a 10 °C/min ramp to 650 °C, and ending with a 5 min isothermal phase; 20 mL/min dry air. Sample weight: ∼5−20 mg. A mass spectrometer, connected to TGA exhaust, was initiated at the beginning of the TPO phase to gather CO_2 evolution signals. An example TGA curve is shown in Figure S12.

The exhaust gases from the TGA were connected via a capillary tube to the inlet of a Stanford Research Systems UGA200 Universal Gas Analyzer equipped with a mass spectrometer. Pressure vs time scans at ∼2 s intervals were collected by UGA during the temperature programmed oxidation (TPO) phase of the TGA regimen (Figure S8), scanning for nitrogen (28 amu), carbon dioxide (44 amu), and oxygen (32 amu). The gas residence time from a TGA furnace to an UGA output signal was calculated by measuring the delay time from switching from nitrogen to air until an initial rise in the UGA oxygen signal was detected. In addition, the rise time from the initial increase in oxygen signal until reaching steady state after switching gas flow was measured. The residence time was calculated as the delay time plus one-half of the rise time. This residence time was used to time align the UGA signals with the TGA signals. The UGA carbon dioxide signal (in Torr) baseline was zeroed, and the signal was calibrated using activated carbon in the TGA. The mass loss measured in the TGA (in mg of carbon) was linked to the corresponding UGA carbon dioxide signal area in Torr·s. See Figure S11 for a sample TGA-MS trace.

■ ASSOCIATED CONTENT

Supporting Information

The Supporting Information is available free of charge at https://pubs.acs.org/doi/10.1021/acssuschemeng.3c02202.

Powder X-ray diffraction (PXRD) patterns of screened and postreaction catalysts, N_2 physisorption isotherms of screened and postreaction catalysts, details of thermogravimetric analysis (TGA) program and curves, and detailed mass balances of hydrogenolysis reactions (PDF)

■ AUTHOR INFORMATION

Corresponding Author

Manish Shetty − *Artie McFerrin Department of Chemical Engineering, Texas A&M University College Station, College Station, Texas 77843, United States;* orcid.org/0000-0002-8611-7415; Email: manish.shetty@tamu.edu

Authors

Siddhesh S Borkar − *Artie McFerrin Department of Chemical Engineering, Texas A&M University College Station, College Station, Texas 77843, United States*

Ryan Helmer − *Artie McFerrin Department of Chemical Engineering, Texas A&M University College Station, College Station, Texas 77843, United States*

Suraj Panicker − *Artie McFerrin Department of Chemical Engineering, Texas A&M University College Station, College Station, Texas 77843, United States*

Complete contact information is available at: https://pubs.acs.org/10.1021/acssuschemeng.3c02202

Author Contributions

‡S.S.B. and R.H.: These authors contributed equally.

Author Contributions

The manuscript was written through the contributions of all authors. All authors have given approval for the final version of the manuscript.

Notes

The authors declare no competing financial interest.

■ ACKNOWLEDGMENTS

We are grateful to the Artie McFerrin Department of Chemical Engineering at Texas A&M University, the College of Engineering, Dr. Mark Barteau, and the Provost for their financial support. This work was funded by Texas A&M University (TAMU), Texas A&M Engineering Experiment Station (TEES), and the Governor's University Research Initiative (GURI). M.S. acknowledges support from the Oak Ridge Associated Universities through their Ralph E. Powe Junior Faculty Enhancement Award. We thank Yinying Hua, Donga Kang, and Denis Johnson for assisting with collecting powder X-ray diffraction patterns of pre- and postreaction samples. We also acknowledge that the microscopy characterization of the catalyst powders was performed in the Texas A&M University Materials Characterization Core Facility (RRID:SCR_022202).

■ REFERENCES

(1) Geyer, R.; Jambeck, J. R.; Law, K. L. Production, use, and fate of all plastics ever made. *Science Advances* **2017**, *3* (7), No. e1700782.

(2) Rahimi, A.; García, J. M. Chemical recycling of waste plastics for new materials production. *Nature Reviews Chemistry* **2017**, *1* (6), 0046.

(3) Celik, G.; Kennedy, R. M.; Hackler, R. A.; Ferrandon, M.; Tennakoon, A.; Patnaik, S.; LaPointe, A. M.; Ammal, S. C.; Heyden, A.; Perras, F. A.; et al. Upcycling Single-Use Polyethylene into High-Quality Liquid Products. *ACS Central Sci.* **2019**, *5* (11), 1795−1803.

(4) Cozar, A.; Echevarria, F.; Gonzalez-Gordillo, J. I.; Irigoien, X.; Ubeda, B.; Hernandez-Leon, S.; Palma, A. T.; Navarro, S.; Garcia-de-Lomas, J.; Ruiz, A.; Fernandez-de-Puelles, M. L.; Duarte, C. M.; et al. Plastic debris in the open ocean. *Proc. Natl. Acad. Sci. U.S.A.* **2014**, *111* (28), 10239−10244.

(5) Mark, L. O.; Cendejas, M. C.; Hermans, I. The Use of Heterogeneous Catalysis in the Chemical Valorization of Plastic Waste. *ChemSusChem* **2020**, *13* (22), 5808−5836.

(6) Law, K. L. Plastics in the Marine Environment. *Annual Review of Marine Science* **2017**, *9*, 205−229.

(7) Zhang, F.; Zeng, M. H.; Yappert, R. D.; Sun, J. K.; Lee, Y. H.; LaPointe, A. M.; Peters, B.; Abu-Omar, M. M.; Scott, S. L. Polyethylene upcycling to long-chain alkylaromatics by tandem hydrogenolysis/aromatization. *Science* **2020**, *370* (6515), 437−441.

(8) Chamas, A.; Moon, H.; Zheng, J.; Qiu, Y.; Tabassum, T.; Jang, J. H.; Abu-Omar, M.; Scott, S. L.; Suh, S. Degradation Rates of Plastics in the Environment. *ACS Sustainable Chem. Eng.* **2020**, *8* (9), 3494−3511.

(9) Wang, C.; Liu, Y.; Chen, W.-Q.; Zhu, B.; Qu, S.; Xu, M. Critical review of global plastics stock and flow data. *Journal of Industrial Ecology* **2021**, *25* (5), 1300−1317.

(10) Schyns, Z. O. G.; Shaver, M. P. Mechanical Recycling of Packaging Plastics: A Review. *Macromol. Rapid Commun.* **2021**, *42* (3), No. 2000415.

(11) Borkar, S. S.; Helmer, R.; Mahnaz, F.; Majzoub, W.; Mahmoud, W.; Al-Rawashdeh, M. m.; Shetty, M. Enabling resource circularity through thermo-catalytic and solvent-based conversion of waste plastics. *Chem Catalysis* **2022**, *2* (12), 3320−3356.

(12) IEA. *Production of key thermoplastics, 1980−2050*; 2020; https://www.iea.org/data-and-statistics/charts/production-of-key-thermoplastics-1980-2050.

(13) Peacock, A. J. THE CHEMISTRY OF POLYETHYLENE*. *Journal of Macromolecular Science, Part C* **2001**, *41* (4), 285−323.

(14) Chen, X.; Wang, Y. D.; Zhang, L. Recent Progress in the Chemical Upcycling of Plastic Wastes. *ChemSusChem* **2021**, *14* (19), 4137−4151.

(15) Kots, P. A.; Vance, B. C.; Vlachos, D. G. Polyolefin plastic waste hydroconversion to fuels, lubricants, and waxes: a comparative study. *Reaction Chemistry & Engineering* **2021**, *7*, 41.

(16) Rorrer, J. E.; Beckham, G. T.; Roman-Leshkov, Y. Conversion of Polyolefin Waste to Liquid Alkanes with Ru-Based Catalysts under Mild Conditions. *JACS Au* **2021**, *1* (1), 8−12.

(17) Dufaud, V.; Basset, J. M. Catalytic Hydrogenolysis at Low Temperature and Pressure of Polyethylene and Polypropylene to Diesels or Lower Alkanes by a Zirconium Hydride Supported on Silica-Alumina: A Step Toward Polyolefin Degradation by the Microscopic Reverse of Ziegler-Natta Polymerization. *Angew. Chem., Int. Ed.* **1998**, *37* (6), 806−810.

(18) Mason, A. H.; Motta, A.; Das, A.; Ma, Q.; Bedzyk, M. J.; Kratish, Y.; Marks, T. J. Rapid atom-efficient polyolefin plastics hydrogenolysis mediated by a well-defined single-site electrophilic/cationic organo-zirconium catalyst. *Nature Communications* **2022**, *13* (1), 7187.

(19) Jia, C.; Xie, S.; Zhang, W.; Intan, N. N.; Sampath, J.; Pfaendtner, J.; Lin, H. Deconstruction of high-density polyethylene into liquid hydrocarbon fuels and lubricants by hydrogenolysis over Ru catalyst. *Chem Catalysis* **2021**, *1* (2), 437−455.

(20) Kots, P. A.; Liu, S.; Vance, B. C.; Wang, C.; Sheehan, J. D.; Vlachos, D. G. Polypropylene Plastic Waste Conversion to Lubricants over Ru/TiO2 Catalysts. *ACS Catalysis* **2021**, *11* (13), 8104−8115.

(21) Rorrer, J. E.; Troyano-Valls, C.; Beckham, G. T.; Román-Leshkov, Y. Hydrogenolysis of Polypropylene and Mixed Polyolefin Plastic Waste over Ru/C to Produce Liquid Alkanes. *ACS Sustainable Chem. Eng.* **2021**, *9* (35), 11661−11666.

(22) Helmer, R.; Shetty, M. Toward a unified metric of catalyst comparison in polymer hydrogenolysis. *Chem Catalysis* **2023**, *3* (5), 100585.

(23) Jing, Y. X.; Wang, Y. Q.; Furukawa, S. Y.; Xia, J.; Sun, C. Y.; Hulsey, M. J.; Wang, H. F.; Guo, Y.; Liu, X. H.; Yan, N. Towards the Circular Economy: Converting Aromatic Plastic Waste Back to Arenes over a Ru/Nb2O5 Catalyst. *Angewandte Chemie International Edition* **2021**, *60* (10), 5527−5535.

(24) Nakaji, Y.; Tamura, M.; Miyaoka, S.; Kumagai, S.; Tanji, M.; Nakagawa, Y.; Yoshioka, T.; Tomishige, K. Low-temperature catalytic upgrading of waste polyolefinic plastics into liquid fuels and waxes. *Appl. Catal. B: Environ.* **2021**, *285*, 119805.

(25) Wang, C.; Xie, T.; Kots, P. A.; Vance, B. C.; Yu, K.; Kumar, P.; Fu, J.; Liu, S.; Tsilomelekis, G.; Stach, E. A.; et al. Polyethylene Hydrogenolysis at Mild Conditions over Ruthenium on Tungstated Zirconia. *JACS Au* **2021**, *1* (9), 1422−1434.

(26) Ertem, S. P.; Onuoha, C. E.; Wang, H. Q.; Hillmyer, M. A.; Reineke, T. M.; Lodge, T. P.; Bates, F. S. Hydrogenolysis of Linear Low-Density Polyethylene during Heterogeneous Catalytic Hydrogen-Deuterium Exchange. *Macromolecules* **2020**, *53* (14), 6043−6055.

(27) Liu, S. B.; Kots, P. A.; Vance, B. C.; Danielson, A.; Vlachos, D. G. Plastic waste to fuels by hydrocracking at mild conditions. *Science Advances* **2021**, *7* (17), 9.

(28) Sun, M.; Zhu, L.; Liu, W.; Zhao, X.; Zhang, Y.; Luo, H.; Miao, G.; Li, S.; Yin, S.; Kong, L. Efficient upgrading of polyolefin plastics into C5−C12 gasoline alkanes over a Pt/W/Beta catalyst. *Sustainable Energy & Fuels* **2022**, *6*, 271.

(29) Tennakoon, A.; Wu, X.; Paterson, A. L.; Patnaik, S.; Pei, Y. C.; LaPointe, A. M.; Ammal, S. C.; Hackler, R. A.; Heyden, A.; Slowing, I. I.; et al. Catalytic upcycling of high-density polyethylene via a processive mechanism. *Nat. Catal.* **2020**, *3* (11), 893−901.

(30) Utami, M.; Wijaya, K.; Trisunaryanti, W. Pt-promoted sulfated zirconia as catalyst for hydrocracking of LDPE plastic waste into liquid fuels. *Mater. Chem. Phys.* **2018**, *213*, 548−555.

(31) Vance, B. C.; Kots, P. A.; Wang, C.; Hinton, Z. R.; Quinn, C. M.; Epps, T. H.; Korley, L. T. J.; Vlachos, D. G. Single pot catalyst strategy to branched products via adhesive isomerization and hydrocracking of polyethylene over platinum tungstated zirconia. *Appl. Catal. B: Environ.* **2021**, *299*, 120483.

(32) Wu, X.; Tennakoon, A.; Yappert, R.; Esveld, M.; Ferrandon, M. S.; Hackler, R. A.; LaPointe, A. M.; Heyden, A.; Delferro, M.; Peters, B.; et al. Size-Controlled Nanoparticles Embedded in a Mesoporous Architecture Leading to Efficient and Selective Hydrogenolysis of Polyolefins. *J. Am. Chem. Soc.* **2022**, *144* (12), 5323−5334.

(33) Jaydev, S. D.; Usteri, M.-E.; Martín, A. J.; Pérez-Ramírez, J. Identifying selective catalysts in polypropylene hydrogenolysis by decoupling scission pathways. *Chem Catalysis* **2023**, 3 (5), 100564.

(34) Critical mineral resources of the United States—Economic and environmental geology and prospects for future supply. *U.S. Geological Survey Professional Paper 1802*; USGS: Reston, VA, 2017; http://pubs.er.usgs.gov/publication/pp1802; DOI: 10.3133/pp1802.

(35) Emsley, J. *Nature's building blocks: an A-Z guide to the elements*; Oxford University Press, 2003.

(36) Vance, B. C.; Kots, P. A.; Wang, C.; Granite, J. E.; Vlachos, D. G. Ni/SiO2 catalysts for polyolefin deconstruction via the divergent hydrogenolysis mechanism. *Appl. Catal. B-Environ.* **2023**, *322*, 122138.

(37) Zichittella, G.; Ebrahim, A. M.; Zhu, J.; Brenner, A. E.; Drake, G.; Beckham, G. T.; Bare, S. R.; Rorrer, J. E.; Román-Leshkov, Y. Hydrogenolysis of Polyethylene and Polypropylene into Propane over Cobalt-Based Catalysts. *JACS Au* **2022**, *2* (10), 2259−2268.

(38) Chen, S.; Tennakoon, A.; You, K.-E.; Paterson, A. L.; Yappert, R.; Alayoglu, S.; Fang, L.; Wu, X.; Zhao, T. Y.; Lapak, M. P.; et al. Ultrasmall amorphous zirconia nanoparticles catalyse polyolefin hydrogenolysis. *Nat. Catal.* **2023**, *6* (2), 161−173.

(39) Chen, L.; Zhu, Y.; Meyer, L. C.; Hale, L. V.; Le, T. T.; Karkamkar, A.; Lercher, J. A.; Gutiérrez, O. Y.; Szanyi, J. Effect of reaction conditions on the hydrogenolysis of polypropylene and polyethylene into gas and liquid alkanes. *Reaction Chemistry & Engineering* **2022**, 7 (4), 844−854.

(40) Gierada, M.; De Proft, F.; Sulpizi, M.; Tielens, F. Understanding the Acidic Properties of the Amorphous Hydroxylated Silica Surface. *The Journal of Physical Chemistry C* **2019**, *123* (28), 17343−17352.

(41) Collins, C. D. Implementing Phytoremediation of Petroleum Hydrocarbons. In *Phytoremediation: Methods and Reviews*, Willey, N. Ed.; Humana Press, 2007; pp 99−108.

(42) Young, R. J.; Lovell, P. A. *Introduction to Polymers*; CRC Press, 2011.

(43) Storsæter, S.; Chen, D.; Holmen, A. Microkinetic modelling of the formation of C1 and C2 products in the Fischer−Tropsch synthesis over cobalt catalysts. *Surf. Sci.* **2006**, *600* (10), 2051−2063.

(44) Hill, C. G.; Root, T. W. *Introduction to Chemical Engineering Kinetics and Reactor Design*, 2nd ed.; Wiley, 2014.

(45) Kissin, Y. V. Relative reactivities of alkanes in catalytic cracking reactions. *J. Catal.* **1990**, *126* (2), 600−609.

(46) Kissin, Y. V. Kinetics of alkane adsorption on a solid cracking catalyst. *Journal of Molecular Catalysis A: Chemical* **1998**, *132* (1), 101−112.

(47) Bhadra, B. N.; Jhung, S. H. Selective Adsorption of n-Alkanes from n-Octane on Metal-Organic Frameworks: Length Selectivity. *ACS Appl. Mater. Interfaces* **2016**, *8* (10), 6770−6777.

(48) Haynes, W. M.; Lide, D. R.; Bruno, T. J. *CRC Handbook of Chemistry and Physics*; CRC Press, 2014.

(49) Sam, S. T.; Nuradibah, M. A.; Ismail, H.; Noriman, N. Z.; Ragunathan, S. Recent Advances in Polyolefins/Natural Polymer Blends Used for Packaging Application. *Polymer-Plastics Technology and Engineering* **2014**, *53* (6), 631−644.

(50) Şahan, H.; Göktepe, H.; Yıldız, S.; Çaymaz, C.; Patat, Ş. A novel and green synthesis of mixed phase CoO@Co3O4@C anode material for lithium ion batteries. *Ionics* **2019**, *25* (2), 447−455.

(51) Su, D.; Dou, S.; Wang, G. Single Crystalline Co3O4 Nanocrystals Exposed with Different Crystal Planes for Li-O2 Batteries. *Scientific Reports* **2014**, *4* (1), 5767.

(52) Park, S.; Kim, S. J.; Oh, K. C.; Cho, L.; Jeon, Y.; Lee, C.; Kim, D. Thermogravimetric analysis-based proximate analysis of agro-byproducts and prediction of calorific value. *Energy Reports* **2022**, *8*, 12038−12044.

(53) Choudhary, J.; Alawa, B.; Chakma, S. Insight into the kinetics and thermodynamic analyses of co-pyrolysis using advanced isoconversional method and thermogravimetric analysis: A multi-model study of optimization for enhanced fuel properties. *Process Safety and Environmental Protection* **2023**, *173*, 507−528.

(54) Querini, C. A.; Fung, S. C. Temperature-programmed oxidation technique: kinetics of coke-O2 reaction on supported metal catalysts. *Appl. Catal. A: General* **1994**, *117* (1), 53−74.

(55) Prasomsri, T.; Shetty, M.; Murugappan, K.; Román-Leshkov, Y. Insights into the catalytic activity and surface modification of MoO3 during the hydrodeoxygenation of lignin-derived model compounds into aromatic hydrocarbons under low hydrogen pressures. *Energy & Environmental Science* **2014**, 7 (8), 2660−2669.

(56) Querini, C. A.; Fung, S. C. Coke characterization by temperature programmed techniques. *Catal. Today* **1997**, *37* (3), 277−283.

(57) Li, Z. j.; Liu, C. r.; Zhao, Q. s. Effect of heat treatment on the pore structure properties of silica gel powders derived from water glass. *J. Non-Cryst. Solids* **2000**, *265* (1), 189−192.

(58) Brunauer, S.; Emmett, P. H.; Teller, E. Adsorption of Gases in Multimolecular Layers. *J. Am. Chem. Soc.* **1938**, *60* (2), 309−319.

(59) *Anton Paar QuantaTec Instruction Manual and Safety Information for autosorb iQ Gas Sorption System*; Anton Paar: Graz, Austria, 2022.

(60) de Saint Laumer, J. Y.; Leocata, S.; Tissot, E.; Baroux, L.; Kampf, D. M.; Merle, P.; Boschung, A.; Seyfried, M.; Chaintreau, A. Prediction of response factors for gas chromatography with flame ionization detection: Algorithm improvement, extension to silylated compounds, and application to the quantification of metabolites. *J. Sep. Sci.* **2015**, *38* (18), 3209−3217.